Titanium Dioxide and Hematite Based Photoelectrodes for Photoelectrochemical Water Splitting

QUAID-I-AZAM UNIVERSITY
ISLAMABAD

A thesis submitted to the Department of Chemistry, Quaid-i-Azam University Islamabad, in partial fulfilment of the requirement for the degree of

Doctor of Philosophy
In
Inorganic/Analytical Chemistry

By
Abrar Ahmad
Department of Chemistry
Quaid-i-Azam University
Islamabad 45320, Pakistan
(2021)

DECLARATION

This is to certify that this dissertation entitled ***"Titanium Dioxide and Hematite Based Photoelectrodes for Photoelectrochemical Water Splitting"*** submitted by ***Mr. Abrar Ahmad,*** is accepted in its present form by the Department of Chemistry, Quaid-i-Azam University, Islamabad, Pakistan, as satisfying the partial requirement for the award of degree of ***Doctor of Philosophy in Analytical/Inorganic Chemistry.***

External Examiner (I):
Prof. Dr. Mrs. Uzaira Rafique
Dean Faculty of Science & Technology
Fatima Jinnah Women University
Rawalpindi.

External Examiner (II):
Dr. Moazzam Hussain Bhatti
Associate Professor
Department of Chemistry
Allama Iqbal Open University
H-8, Islamabad.

Supervisor :
Prof. Dr. Zia-ur-Rehman
Department of Chemistry
Quaid-i-Azam University
Islamabad.

Head of Section:
Prof. Dr. Mrs. Zareen Akhter
Department of Chemistry
Quaid-i-Azam University
Islamabad.

Chairman:
Prof. Dr. Aamer Saeed Bhatti
Department of Chemistry
Quaid-i-Azam University
Islamabad.

Certificate of Approval

This is to certify that the research work presented in this thesis, entitled "**Titanium Dioxide and Hematite Based Photoelectrodes for Photoelectrochemical Water Splitting**" was conducted by **Mr. Abrar Ahmad** under the supervision of **Prof. Dr. Zia-ur-Rehman**

No part of this thesis has been submitted any where else for any other degree. This thesis, is submitted to the **Department of Chemistry Quaid-i-Azam University Islamabad** in partial fulfillment of the requirements for the Doctor of Philosophy in Field of **Analytical/Inorganic Chemistry Department of Chemistry, Quaid-i-Azam University, Islamabad.**

Student Name Mr. Abrar Ahmad Signature:

Examination Committee:

1. **External Examiner:** **Prof. Dr. Mrs. Uzaira Rafique** Signature:
Dean Faculty of Science & Technology
Fatima Jinnah Women University
Rawalpindi.

2. **External Examiner:** **Dr. M. Moazzam Hussain Bhatti** Signature:
Associate Professor
Department of Chemistry
Allama Iqbal Open University
H-8, Islamabad

3. **Internal Examiner:** **Prof. Dr. Mrs. Zareen Akhter** Signature:
Department of Chemistry
Quaid-i-Azam University
Islamabad.

Supervisor: **Prof. Dr. Zia-ur-Rehman** Signature:

Head of Department: **Prof. Dr. Aamer Saeed Bhatti** Signature:

The Art of writing only for samples use

PLAGIARISM UNDERTAKING

I solemnly declare that, the research work presented in the thesis titled "**Titanium Dioxide and Hematite Based Photoelectrodes for Photoelectrochemical Water Splitting**" is solely my research work with no significant contribution from any other person. Small contribution/help wherever taken has been duly acknowledged and that complete thesis has been written by me.

I understand the zero tolerance policy of the HEC and **Quaid-i-Azam University Islamabad** towards plagiarism. Therefore, I as an Author of the above titled thesis declare that no portion of my thesis has been plagiarized and any material used as reference is properly referred/cited.

I undertake that if I am found guility of any formal plagiarism in the above titled thesis even after award of Ph.D. degree, the university reserves the rights to withdraw/revoke my Ph.D. degree and that HEC and the University has the right to publish my name on the HEC/University website on which names of students are placed who submitted plagiarized thesis.

Student/Author Signature:

Name: **Mr. Abrar Ahmad**

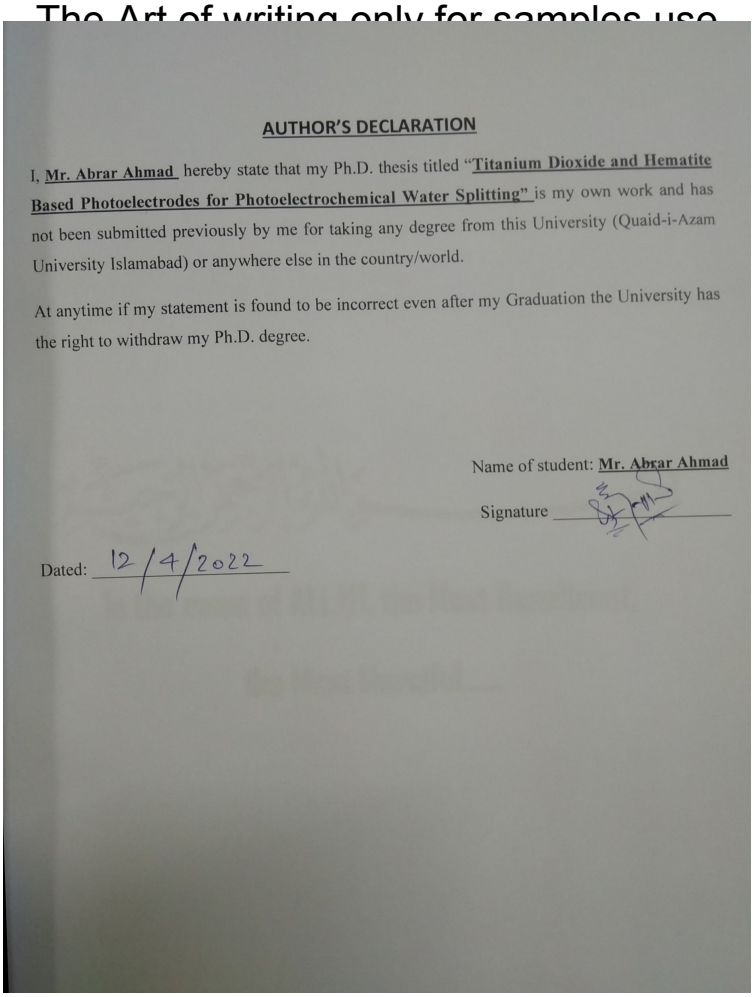

AUTHOR'S DECLARATION

I, **Mr. Abrar Ahmad** hereby state that my Ph.D. thesis titled "**Titanium Dioxide and Hematite Based Photoelectrodes for Photoelectrochemical Water Splitting**" is my own work and has not been submitted previously by me for taking any degree from this University (Quaid-i-Azam University Islamabad) or anywhere else in the country/world.

At anytime if my statement is found to be incorrect even after my Graduation the University has the right to withdraw my Ph.D. degree.

Name of student: **Mr. Abrar Ahmad**

Signature _____

Dated: 12/4/2022

بسم الله الرحمن الرحيم

In the name of ALLAH, the Most Beneficent,

the Most Merciful.....

"Whoever travels a path in search of knowledge, Allah will make easy for him a path to Paradise."

Prophet Muhammad (PBUH)

Source: Sahih Muslim 2699

Dedicated to my loving family

They were there when and where I need them.

ACKNOWLEDGEMENT

First and foremost, I praise **Almighty Allah** who bestowed me with wellbeing, endurance, capability to think, and strength to execute this project successfully. All respects to **Holy Prophet Hazrat Muhammad** (Peace be upon him) who urged his followers to pursue knowledge from cradle to grave and who enable us to recognize our creator.

Many exceptional people supported and guided me directly or indirectly throughout this research journey. Though it is hard to mention all of them, I owe them my appreciation and gratitude. I am highly thankful to my reverent supervisor **Dr. Zia-ur-Rehman** for his kind cooperation, useful suggestions, thought-provoking guidance, encouraging attitude, pleasant behavior, and taking a keen interest in this project. Besides, I am grateful to **Prof. Dr. Aamer Saeed Bhatti** (Chairman Department of Chemistry), **Prof. Dr. Zareen Akhter** (Head of inorganic/Analytical section), and the whole staff of the department of chemistry, Quaid-i- Azam University, Islamabad, for their assistance and granted me a fruitful and productive climate for my project.

Above all, I would like to show my thankfulness to the Republic of Turkey, The Scientific and Technological Research Council of Turkey, and Çukurova University, Adana, Turkey for offering me the precious opportunity to perform a part of my Ph.D. work in this amazing country and institute. I am highly grateful to my host supervisor **Prof. Dr. Gülfeza Kardaş** (Chemistry Department, Çukurova University, Adana, Turkey) for her continuous support, encouragement, constructive input, and guidance. Thank you for everything. It was a great privilege working with you. To be honest, this study would not be accomplished without your assistance and instruction. Also, my earnest appreciation goes to, **Prof. Dr. Halime Paksoy** (Chemistry Department, Çukurova University) for her timely, constructive feedback and insightful guidance during my stay at Çukurova University.

I am also grateful for the support and the friends I made at the Chemistry Department, Çukurova University, Adana, Turkey. I feel lucky to work with **Dr. Gurbet**

Yerlikaya and **Dr. Fatih Tezcan** great electrochemists and great persons**.** You people have opened for me a different window on chemistry.

I am indebted to **Dr. Hamid Nawaz** for assisting and guiding me through the early stages of my research. Of course, my gratitude and thanks to Lab 42's two excellent gentlemen, **Dr. Jamal Abdul Nasir,** and **Haseeb Ullah** you are not just colleagues for me, you are real friends, you are the best I could ask for. Also, I want to express my thankfulness to every one of the Zia group's former and current members for their supportive attitude, Valuable suggestions, and work discussion during my studies.

I would like to express my heartfelt gratitude to all of my friends at Quaid-i-Azam University and beyond: to convey my special thanks to all my friends in and outside Quaid-i-Azam University: **Dr. Umair shamraiz**, **Zakir Zaman khan**, **Muhammad Nasir Hussain**, **Zahid Nawaz**, **Mobeen Butt, Jehangir Ali**, **Noor Uddin**, **Muhammad Sufiyan, Adnan khalid, Iltaf-ud-din, Yasir Karim khan, Haseen Ahmad, Zakir khan, Zahid Ghassan, Muhammad Atif, Yaqoob Adam, Saeed Baber, Fathul bari, Navid Aziz, Shuja-Ur-Rehman, Ihtiram-ul-Haq, Mehboob-Ur-Rehman, and Waqar Azeem,** for their continuous support, insightful guidance, and cooperation they extended throughout this long journey.

Last but not the least, my love and deepest gratefulness go to my parents and family members for their unending love, unconditional emotional support, and constant encouragement. I express my heartfelt gratitude and submit my earnest thanks to my uncles (**Dr. Nazir Hussain shah, Dr. Gulzar Ahmad, Dr. Rehmat Aman, Dr. Siddique Ahmad, and Riaz Ahmad**) my brothers (**Aftab Ahmad, Arshad Jaffar, Ali Ahmad, and Akhlaq Ahmad**) my cousins (**Fahim Ahmad, Zeeshan Nazir, Saleh Aman, Masroor Hussain, Hussain Ahmad, Hassan ahmad)** and my sisters. Last but not least, I'd want to express my sincerest gratitude to my wife **Faryal Faizi**, for her patience and support during the writing of my thesis. May Almighty ALLAH provide them good health and long and successful life, and may they be a source of prayer for me.

Abrar Ahmad (MR.)

ABSTRACT

To properly utilize solar light for sustainable energy generation, various efforts are being made to overcome the natural diurnal fluctuation and diffuse nature of sunlight. Hydrogen production using a photoelectrochemical (PEC) water splitting setup is a promising approach for harvesting solar energy. To attain good efficiency and durability, the materials used as photoelectrode for PEC water splitting must satisfy a variety of thermodynamic and kinetics parameters. Up till now, there is not a single photoelectrode material that can satisfy the foregoing requirements. So, the search is continuing to obtain a photoelectrode of the requisite properties by tailoring the optical, and electrical properties of the existing photoelectrode. Herein, the PEC performance of Titanium dioxide (TiO_2) and Hematite (α-Fe_2O_3) based photoelectrodes were investigated for water oxidation reactions. Both materials were selected because of their non-hazardous, widespread, biocompatible, and scalable nature. Due to the inherited large band gap of TiO_2, it can absorb only in the ultra-violet of the solar spectrum, which comprises only 3-5 % of the solar spectrum, thus resulting in poor charge collection and efficiency. Therefore, to modify the band gap and charge production capability of TiO_2 implication of numerous strategies like doping with metal and non-metal, heterojunction formation, and sensitization of TiO_2 with certain narrow bandgap semiconductors have been found effective. Similarly, certain intrinsic limitations associated with α-Fe_2O_3 like its poor reaction kinetics for oxygen evolution reaction (OER), short hole diffusion length (2-4 nm), high carrier recombination rate, and positive conduction band edge relative to the hydrogen redox potential can be overcome by coupling it with certain low band gap semiconductors.

The first part of this dissertation includes the synthesis of the three-dimensional double-layered rosette-rod TiO_2 (RT) heterojunction with bismuth sulfide (Bi_2S_3) using two-step hydrothermal and solvothermal routes (RT_Bi_2S_3 X). A seed layer approach is also used to assist the uniform distribution of Bi_2S_3 and to form a perfect heterojunction between TiO_2 (RT) and Bi_2S_3. Morphological studies have revealed the double-layered rosette-rod TiO_2 (RT) architecture consists of two main parts, a one-dimensional

TiO_2 nanorod arrays (NRAs) at the bottom for direct transfer of photoinduced electron and hole pairs, while the upper three-dimensional nano rosette composed of small TiO_2 nanorods as building units to enhance the surface area and light-harvesting efficiency. Morphology of Bi_2S_3 was found to be affected to some extent by the solvothermal duration and the presence of the seed layer. PEC performance at 1.23 V_{RHE} bias-potential under 100 $mWcm^{-2}$ solar light illumination has shown that RT_Bi_2S_3 12h (solvothermal duration 12 hours) photoanode synthesized with a seed layer has the highest photocurrent density of 3.98 $mAcm^{-2}$ at 1.23 VRHE, 10 times, and 5.5 times superior to bare rosette-rod (RT = 0.39 $mAcm^{-2}$ at 1.23 VRHE) and RT_$Bi_2S_3$12h photoanode without the seed layer (0.74 mA cm^{-2} at 1.23 VRHE), respectively. Interestingly, the photocurrent density of RT_Bi_2S_3 12 h photoanode, to the best of our knowledge, is above all the previously used TiO_2 and Bi_2S_3 based photoanodes.

In the second part, the PEC performance of manganese (Mn) doped cadmium sulfide (CdS) quantum dots (QDs) sensitized double-layered rosette-rod TiO_2 (RT) photoanodes have been described. The rosette-rod TiO_2 (RT) architecture was synthesized by the two-step hydrothermal method while Mn-doped CdS QDs sensitization was done by successive ionic layer adsorption and reaction (SILAR) approach. PEC performance of the as-prepared photoanodes, obtained by varying Mn concentration in CdS QDs and the number of the SILAR cycles, are explored in terms of photocurrent density and applied biased to photon conversion efficiency. PEC studies show that the optimized Mn-doped CdS QDs sensitized rosette-rod TiO_2 (RT) photoanode (Mn-CdS\RT(35Mm)-8Cy) shows a maximum photocurrent density of 2.73 $mAcm^{-2}$ at 1.23 VRHE which is 7 times superior to that of bare rosette-rod TiO_2 (RT) photoanode (RT = 0.39 $mAcm^{-2}$ at 1.23 VRHE).

In the third part, the PEC performance of gadolinium (Gd) doped one-dimensional rutile phase TiO_2 NRAs photoelectrodes is being explored. Morphological studies have revealed that part of the Gd in the form of Gadolinia (Gd_2O_3) microspheres are being uniformly distributed on the surface of TiO_2 NRA. These gadolinia microspheres play an important role in a passivation layer reducing the surface recombination of

photogenerated electrons and holes. Linear sweep voltammetry results have shown that Gd doping results in a two-fold escalation in the photocurrent density as compared to pristine TiO_2 NRAs. Mott-Schotty measurements have shown that Gd doping [TiO_2 NRAs (Gd@TiO_2 NRA)] shifted the flat-band potential of TiO_2 NRAs more toward the negative side that resulting in effective charge separation and transportation.

In the final part of this research dissertation, the PEC performance of crisscross α-Fe_2O_3 nanorods (NRs) decorated with Bi_2S_3 nanoparticles (α-Fe_2O_3/Bi_2S_3) for the improved water oxidation reaction is being studied. Bi_2S_3 nanoparticles were tethered to the surface of crisscross α-Fe_2O_3 NRs by combining the SILAR and solvothermal approaches. The former approach is being used for the uniform distribution of Bi_2S_3 on α-Fe_2O_3 NRs to make a better heterojunction contact with few defects. The physicochemical, electrochemical, and optical characterization of α-Fe_2O_3/Bi_2S_3 heterojunctions has revealed its high crystalline nature and presence of two distant phases with different bandgap positions. Linear sweep voltammetry results show that the optimized α-Fe_2O_3/Bi_2S_3 6 h photoanode shows a maximum photocurrent density of 2.550 $mAcm^{-1}$ at 1.23V $_{RHE}$, which is almost 20 times higher than the pristine α-Fe_2O_3 photoanode (0.123 $mAcm^{-1}$ at 1.23V $_{RHE}$).

CONTENTS

List of Figures

The Art of writing only for samples use

The Art of writing only for samples use

The Art of writing only for samples use

List of Tables

The Art of writing only for samples use

The Art of writing only for samples use

List of Schemes

The Art of writing only for samples use

List of Abbreviations

Anodized Alumina Oxide	AAO
Aerosol Assisted Chemical vapour deposition	AACVD
Atomic layer deposition	ALD
Silver/Silver chloride	Ag/AgCl
Atomized spray pyrolysis deposition	ASPD
Conduction Band	CB
Chemical bath deposition	CBD
Cobalt phosphate group	Co-Pi
Carbon nitride quantum dots	CNQDs
Carbon nanotubes	CNTs
Chemical vapour deposition	CVD
Dye-sensitized solar cell	DSSC
Electrospray deposition	ESD
Flat band potential	E_{fb}
Fermi level	E_f
Fluorine-doped Tin Oxide	FTO
Flame Assisted Chemical vapour deposition	FACVD
Greenhouse gases	GHG
General Motors	GM
Hierarchical heterojunction array	HHA
Hydrothermal	HT
International Renewable energy Agency	IRENA
Indium Tin Oxide	ITO
Lowest unoccupied molecular orbital	LUMO
Localized surface plasmonic resonance	LSPR
Mercaptopropionic acid	MPA
p-merceptophenol	MPH
Million-ton oil equivalent	Mtoe

Multi-walled carbon nanotubes	MWCNT
Nanocone	NCs
Nanodendrite	ND
Nanoflowers	NFs
Nanorods	NRs
Nanorod arrays	NRAs
Nanoparticles	NPs
Nanostructured	NS
Nanotubes	NTs
Nanotubular arrays	NTAs
Nanotube photonic crystal	NTPC
Nanowires	NWs
Nanowires arrays	NWAs
One dimensional	1-D
Pascal	Pa
Photocurrent density	J_{sc}
Photoelectrochemical Cell	PEC
Photoluminescence	PL
Pulsed laser deposition	PLD
Polystyrene	PS
Photovoltaic	PV
Plasmon resonance energy transfer	PRET
Physical Vapour deposition	PVD
Quantum dots	QDs
Redox potential	$E°_{redox}$
Radio-frequency	RF
Reversible hydrogen electrode	RHE
Radiofrequency magnetron sputtering	RFMS
Rosette-Rod	RT
Polarization resistance	R_p
Solution resistance	R_s

Successive ionic layer adsorption and reaction	SILAR
Solvothermal	ST
Spray Pyrolysis	SP
Two dimensional	2-D
Three dimensional	3-D
Tetra Watt	TW
Turnover frequency	TOF
Ultrasonic spray	USP
Ultraviolet,	UV
Valence Band	VB

Chapter 1

Introduction

1.1 Fossil Fuel Trap

Our society, right now, is confronting an overwhelming challenge of increasing global energy demand with time. This increment in energy consumption is due to the exponential increase in world population and industrial upsurge of the developing world [1]. To meet energy demand without a negative influence on the world economy, nations are highly reliant on fossil fuels: coal, oils, and natural gas. Currently, fossil fuel supplies more than 80% of the global energy requirement [2]. Larger energy density, easy storage, and ease of transportation make fossil fuels a perfect source of energy; however, fossil fuels cannot ensure to fulfill our energy requirements forever. The word energy consumption is expected to increase by a factor of 2 from 13.5 TW in 2001 to 27 TW/year up to 2050 and triple by 2100 [3, 4]. At the current utilization rate, the estimated fossil fuel reserves may have vanished within 150 years: approximately 40 years for petroleum, 60 years for natural gas, and coal within 156 years [5]. Declining fuel reserves together with energy insecurity for those nations deprive of fossil fuel reserves highlight the necessity to seek out new renewable energy resources. **Figure 1.1** shows the world's primary energy intake in terms of million-ton oil equivalent (Mtoe) and share of fossil fuel [6].

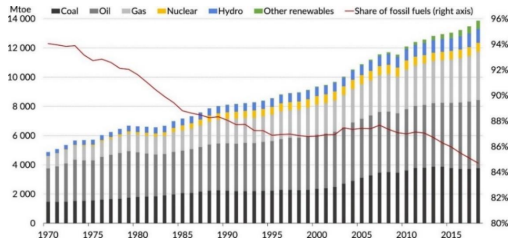

Figure 1.1: World primary energy consumption in terms of million-ton oil equivalent and share of fossil fuel. [6]

On the other side, this wholesale usage of fossil fuels has possibly led to serious environmental concerns, such as the potent greenhouse effect caused by the massive release of carbon dioxide (CO_2) and other greenhouse gases (GHG). About 3×10^{12} kg/year of CO_2, a significant driver of global warming, is added to the atmosphere by the combustion of fossil fuel [7]. Over hundreds of years, the concentration of atmospheric CO_2 has been correlated with global mean temperature and is presently increasing at an unparalleled rate. The main issue is the fact, that an expansive quantity of CO_2 (~98%) on our planet is present in dissolved form in ocean water (7.5×10^{14} kg carbon is present in the atmosphere while 4.1×10^{16} kg carbon is present in ocean water). Almost 2×10^{12} kg of carbon gets liquefied into ocean water every year. The Solubility of CO_2 decreases with an increase in water temperature by around 3% per Kelvin. In case, if there occurs an increase in the mean temperature of the ocean, the CO_2 solubility equilibrium between the ocean and atmosphere will be disturbed [8]. According to the report published by the *Climate Watch* magazine in 2017 worldwide, the average concentration of CO_2 has crossed 405± 0.1ppm, which is believed to be the peak point in the previous 8 x 10^6 years [9, 10]. Baby boomers (born during 1945-65) enjoy low-priced oil and a better environment, X–Gen (born during 1965-80) introduced optimum CO_2 into the environment, Y–Gen (born from 1980 to 2000) start feeling the effect of climate change, while Z –Gen (born after 2000) began suffering from the death spiral of climate change. Prior emission of CO_2 cannot be undone by a simple click, but we can take a step to mitigate and reduce CO_2 emission. X and Y-Gens may not be able to get CO_2 concentration below 400 ppm in their lifetime, Z-Gens may be able to see if all of us are out now to strive against GHG [11]. Subsequently, firm actions should be taken to drastically reduce the emission of CO_2 and other GHG into the atmosphere, otherwise, there will be devastating consequences for the climate. Due to the predictable increase in fuel prices and environmental restrictions, alternative clean and cheap energy sources are desperately needed. The main driver behind the vision of producing energy from sustainable energy resources is (i) to improve the quality of air by reducing CO_2 and other GHG emissions to the atmosphere (ii) to produce energy using local, cheap, and renewable sources (iii) to develop new practical and cost-effective technologies on industrial scale-crucial for our economic growth and

prosperity [12]. **Figure 1.2** shows CO_2 concentration in the atmosphere and mean growth rate (Source: National Oceanic and Atmospheric Administration (NOAA) Mouna Loa).

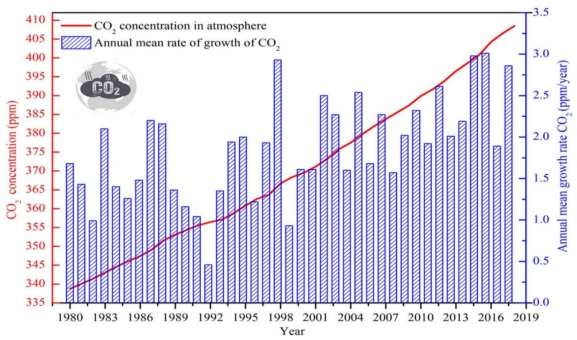

Figure 1.2: CO_2 concentration in the atmosphere and mean growth rate (Source: (NOAA) Mouna Loa). [10]

1.1.1 Clean Energy Systems

The development of a clean and safe energy system other than fossil fuel that can fulfill the worldwide energy request is a vital challenge in the 21st-century [7]. Thus, there is a dire necessity to have a clean and sustainable energy system that can deliver high energy output efficiency and less environmental impact [13]. Clean energy systems should be able to do it using local, cheap, and renewable resources to fulfill the current need. The advantages of a clean energy system can be summarized into three major groups that are social, economic, and environmental. Dincer defined the main components of a clean energy system: (i) suitable output efficiency; (ii) appropriate cost (iii) proper utilization of resources; (iv) improved design and scrutiny (v) effective energy security; and (vi) healthier atmosphere [13, 14].

The Art of writing only for samples use

1.1.2 Renewable Energy Sources

Renewable energy is any energy source that may be regenerated and sustained without any depletion or any severe effect on the environment [15]. Renewable energy sources are broadly regarded as a capable substitute for traditional fossil fuels, hence getting significant attention [2]. Renewable energy sources contribute to 19.1% of the total energy consumption in 2013 [16]. Energy production from renewable energy is increasing day by day and most nations aim to attain more than 15% of their energy production from renewable sources by 2020 [17]. Globally renewable energy produces 19.5 % of our electricity supply [18]. According to the latest scenario, the growth and expansion of the electricity division are headed by the renewable sector; specifically, solar photovoltaic (PV), hydro, and wind sectors. Renewable energy usage is increasing every year by 3.0% [18]. Luckily, renewable energy can be used on a wide scale as its resources are spread universally, compared to traditional fossil fuels which are more geographically concentrated. All nations in the world have at least one abundant renewable energy source, while some countries have a range of various energy resources. As compared to the traditional energy sources, most renewable sources like solar and wind are usually uncertain and fluctuate as solar irradiance intensity and wind speed vary greatly over time and days. Low energy density is considered one of the most annoying drawbacks of renewable energy. It is clear that for a continued energy supply system a single renewable energy source is not sufficient. Therefore, for a continued energy supply, a hybrid renewable energy system should be introduced by integrating various renewable energy sources [19, 20]. Secondly, the increased emission of CO_2 and energy consumption have also compelled the environmental economist and policy analysts to shift their consideration toward the usage of renewable energy sources. As a result, various international associations have started pressurizing several developed and developing countries to lessen the emission of CO_2 [16]. The major geopolitical decision mainly "The Paris Agreement" has demanded a global lessening of CO_2 emissions. According to the IRENA's 2017 Climate-Safe Energy Solution statement to accomplish such a huge objective and significantly bounds the adverse effect of climate change, comprehensive decarbonization of energy use should be done within 50 years. Up to 2060, the world

The Art of writing only for samples use

economy will be triplet so this target cannot be attained without renewable energy sources developing at a minimum of seven-time to the present growth rate (IRENA, 2017) [1]. Therefore, environmental and international pressure, technology, energy insecurity, and deregulated energy market can all play an important part in obtaining a sustainable environmentally friendly route [16]. **Figure 1.3** shows global investment done in renewable energy from 2004 to 2017 (Source: REN2I renewables 2019)[16].

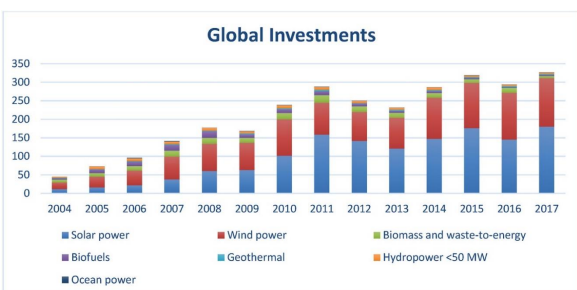

Figure 1.3: Global Investment in renewable energy from 2004 to 2017 (Source: REN2I renewables 2019). [16]

1.1.3 Solar Energy: Pathway to a Carbon-free Future

The utilization of renewable energy resources is the only way to reduce the emission of GHG and other major pollutants into the atmosphere. Long term survival of humankind is highly dependent on the improvement of sustainable and renewable energy resources to remove the dependency on fossil fuels. Amongst all the renewable energy resources available, solar energy is considered a viable replacement for fossil fuels due to its endless and considerable supply. In one year a total of approximately 173000 TW of solar energy is provided by the sun which is 9600 times more than the total annual global energy demand (18.39 TW in 2018) [21]. Presently, solar energy provides only 0.7% of the world's energy supply **(Figure 1.4)** [22].

The Art of writing only for samples use

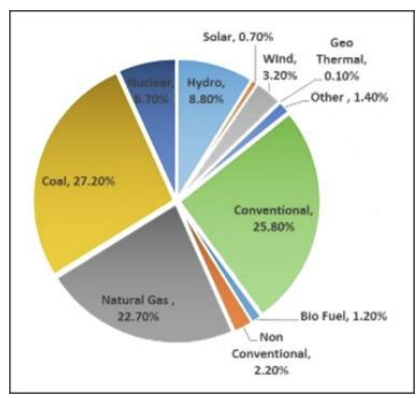

Figure 1.4: World energy scenario. [22]

The transformation of solar energy directly into electricity by using photovoltaic (PV) panels is amongst the most capable markets in the arena of renewable energy sources. In comparison to traditional power production such as using fossil fuel, PV systems do not convey any harmful impact on the ecosystem like air pollution, acid rain, climate change, and so on [23-25]. Secondly, concerning fossil fuels PV energy does not have to be dug out, purified, and conveyed to the production site [26]. Also, in comparison to other renewable energy resources, the PV energy system shows a very little extent of damage to the surroundings from where it is produced, like in case energy generated from hydroelectric plants, the courses of rivers are changed, and a large area is swamped. Another significant aspect is the cost of running which is high for hydroelectric plants as related to the cost for functioning solar power plants [27]**.** In contrast to wind energy, PV energy is noiseless and can be easily used in the metropolitan area also as the PV panel can be fixed on rooftops [24]. PV plants can also be installed on both lands as well as over water bodies. Floating type PV solar panels have a significant advantage as compared to land-based solar panels, including fewer hindrances to obstruct sunlight, appropriate

energy efficiency, and greater power production efficiency because of low temperature under PV panels. Fitting PV solar system over freshwater bodies like lakes also brings advantages to aquatic life such as preventing excess evaporation of water, confining algae growth, and improving water quality**. Figure 1.5** shows the Global accumulated growth of solar power in gigawatts [1, 28]. Besides all these advantages there are certain drawbacks associated with PV solar systems like high initial cost, limitation in availability of PV systems in the market, need relative a large area for installation, dependent on technology development, and highly dependent on geographical location (solar irradiance)[25, 26, 29, 30]. The cost of PV cells is highly influenced by location, a less sunny location requires many solar panels to produce a similar quantity of electricity compared to a minor system in high sunny locations. Similarly, if the PV panel station is far away from the grid a large transmission line is required to attach the power to the grid that increases cost. Cost of the PV system is also influenced by the kind of the technology used and complexity of the system [27, 31-34]. The productivity of the PV Solar system is greatly influenced by temperature, dust, and solar irradiance. The temperature has a drastic effect on the functioning of the solar cell, so various studies are carried out to reduce the temperature by heat extraction and then its utilization for additional causes like heating water or air. Dust also affects the efficiency of the PV system as it blocks the irradiance on the PV modules. Thus, it is advisable to clean the PV solar panel regularly to uphold its performance. Lower the solar irradiance lower will be the cell efficiency as a smaller number of photons reaches the panel surface [27, 31, 35-38]. Secondly, the diurnal nature of solar radiation and variation of sunlight intensity falling on the earth's surface as a function of weather conditions and seasons make it impossible for powering continuously. Therefore, the surplus supply produced during sunlight peak hours should be saved in some other form of energy to be used during nighttime. However, a promising approach to address this problem is to transform and stock solar energy in the form of commercially useful products, as a storage medium for use elsewhere.

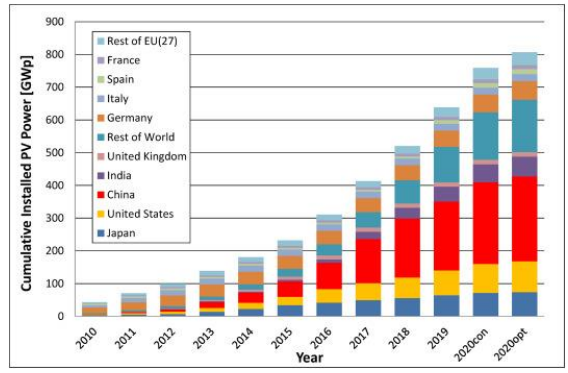

Figure 1.5: Global accumulated growth of solar power in gigawatts. [1, 28]

1.1.4 Hydrogen (H_2) as Fuel for Future

Among the know fuels up to date, H_2 has been marked as a potential fuel to substitute all non-renewable traditional fossil fuels. Due to near-zero or zero-end emissions and continuously renewed resources, H_2 is considered a sustainable energy carrier [39]. Some of the main privileges of using H_2 are: high energy conversion efficiency, production from water with zero CO_2 emission, easy conversion into another form of energy, storage in various forms like liquid, gaseous, or metal hydride (MgH_2) form, easily transportable and have high heating value (HHV) and low heating value (LHV) as compared to conventional fossil fuels [40]. The annual global growth rate by volume for H_2 production was 5.6% from 2011 to 2015 and is growing rapidly [41]. Though the technology of energy generation from H_2 e.g., fuel cells and the combustion engine are fully developed, H_2 production from simple and inexpensive methods is still a crucial challenge. H_2 is a secondary energy carrier since it is not available naturally in elemental form, therefore, it should be produced from other renewable energy sources. H_2 also occurs in various chemical compounds other than H_2O such as hydrocarbons, and biomass that are chemically transformable to H_2 (H_2 is the 9th most plentiful element and compromises

around 0.9 % of the earth's surface) [42, 43]. Until now, nearly all H_2 generation is dependent on raw fossil fuel (48% from natural gas, 30% from oil, and 18% from coal) just 4% of H_2 is merely generated by electrolysis of water [44 45]. Currently, the utmost widely used industrial route for H_2 production is catalytic steam reforming, implying the treatment of gaseous or vaporized hydrocarbon with steam under high temperature (650-950 °C) and pressure (15-40 bar) over nickel-based catalyst. This traditional method of H_2 production itself faces several problems like its endothermic nature, high operation, and maintenance cost. However, by-products formed during steam reforming of natural gas and bio-diesel are also hazardous to the environment [45, 46]. H_2 produced from other techniques like water electrolysis also faces some serious problems like low system efficiency, and expensive nature due to high maintenance and operation cost [47]. Therefore, a new method should be developed to produce H_2 from sustainable sources that are cost-effective as compared to the existing method and technology. These newly invented techniques should be introduced globally by scientists and researchers to overcome the energy barrier as well as environmental-related issues. **Figure 1.6** depicts a schematic representation of the various H_2 production processes [48].

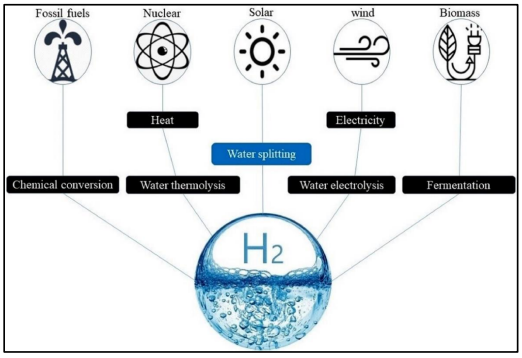

Figure 1.6: Diagrammatic illustration of the various methods used for H_2 production. [48]

1.1.5 Towards a H_2 Economy

The H_2 economy is a hypothetical idea for an infrastructure that is based on H_2 as a principal energy carrier. The term "H_2 economy" was first used by John bockris during his demonstration in 1970 at General Motors (GM) technical center. The main goal of the H_2 economy is to generate H_2 on a grand scale with the help of readily available energy resources to replace the current fossil fuel used in the residential, transport, industrial, and energy sector [5]. The H_2 economy infrastructure consists of five main steps: production, distribution, storage, conversion, and application, almost all of these steps are in various stages of development [49, 50]. The H_2 economy has been considered a comprehensive and permanent solution to the interconnected problems of the developing world like the worldwide environmental issue, shrinking of natural resources, world food scarcity, overpopulation, etc. [5]. Although issues related to fossil fuel economy are highly graved and overwhelmed, therefore, operational development of H_2 economy means incredible advantage for the natural ecology, economy, energy security, and the final consumer [51-53]. Despite indubitable benefits transition from a traditional petroleum-based society toward H_2 based society is fraught with challenges, including the construction of an effective H_2 energy storage system, production issues, distribution networks, and the petroleum market's reaction [54]. Although H_2 has been widely used in refinery and chemical industries, the expense of producing, storing, and transporting H_2 makes it unsuitable for most energy applications [5, 55-57]. Thus, to make the H_2 economy fully developed and to make H_2 a fundamental element of the energy market, serious research and financing should be done to make the H_2 production system more effective, reasonable, consistent, safe, and quick to use for a diverse type of end-user need like large/small scale, static/transportable [58, 59]. However, the huge benefit of the H_2 economy has fascinated many nations to invest immensely to improve the prospect of the energy system [50]. In 2003, the European Union commission high-level group on H_2 and fuel cell technology planned that the European Union will attain an H_2 economy by 2050 and estimated that 35% of the vehicles will be powered by H_2, a zero-carbon fuel, by 2040 [60].

1.1.6 H_2 Production using Solar Energy

The design of novel, simple, inexpensive, and proficient methods for the production of solar fuels is among the leading field of research in solar energy. Among various solar fuels available H_2 has gained a significant position due to its large energy content, environmentally friendly, storage compatibility, and delivery [61-63]. Solar H_2 combines the advantages of fossil fuels (storage and transportation) with the advantages of solar energy (environmental friendliness, renewability, and low risk). Generally, there are five potential methods used to produce solar H_2: solar-thermal, using solar electricity, bio-photolysis, photocatalysis, and photo-electrolysis **(Figure 1.7).**

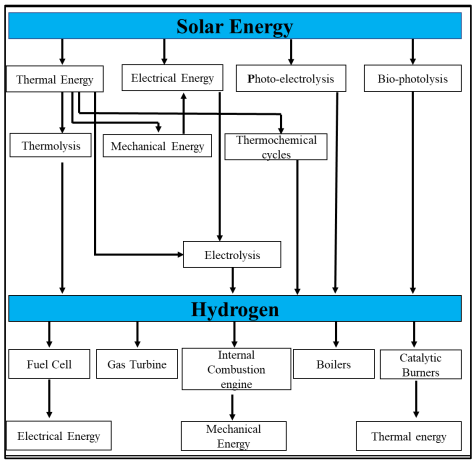

Figure 1.7: Production and utilization of solar H_2 energy. [64]

Solar-thermal H_2 production is further classified into two categories. The first category contains all those techniques where solar thermal energy is used to dissociate

The Art of writing only for samples use

only water or H_2S to generate H_2. While the second category includes methods in which solar thermal energy is used to yield H_2 by the utilization of fossil fuels [65]. One of the main problems associated with solar thermal H_2 production is that further research is needed to develop a high-temperature membrane (necessary for H_2 and oxygen separation to stop their recombination) and heat exchanger [62, 64].

In solar electricity H_2 production, the electricity generated using solar energy is supplied to an electrolyzer where water is electrochemically broken down into H_2 and oxygen. The transformation of solar energy into electricity is carried out by PV cells. While electrolysis of water is done with electrolyzer using current generated by PV cell. PV-based electrolysis is among the costliest methods used for H_2 generation (H_2 produced using PV electrolysis is ~25 times more costly than H_2 produced from fossil fuels). However, after extensive modification and efforts, the cost is now being reduced to 6 times [40, 66, 67].

Photo-biological H_2 production uses a mechanism like photosynthesis found in green algae and plant photosynthesis, however, in it H_2 gas is produced instead of carbon-containing biomass, as is the case in photosynthesis. Two different processes, light-dependent, and light-independent can be used to carry out the biological H_2 production. . The light-dependent process contains direct or indirect bio-photolysis and photo-fermentation. While light-independent processes include fermentation in dark [68]. Photo-biological H_2 production is still in the developmental stage to improve H_2 production yield and to get rid of toxic enzymes involved [64, 69].

Photocatalysis transforms photonic energy obtained from solar irradiation into chemical energy (H_2 fuel). When photons strike a photocatalyst electron-hole pairs are formed, and the generated charges are consumed to split water. To have efficient photocatalytic water splitting the synthesized photocatalyst should have a sufficient band-gap and proper position or potential of conduction and valence band for oxidation/reduction [40]. However, the main problems in photocatalytic water splitting using a heterogeneous catalyst are inefficient charge separation and immediate separation

The Art of writing only for samples use

of H_2 and O_2 from the reaction mixture, and energy consumable process, resulting in low effectiveness of water splitting. Secondly, illumination of the system without quick withdrawal of the photocatalyst results in photo stationary states in which all forward and backward reactions have the same rate, and therefore no further water splitting can be observed [70, 71].

In photo-electrolysis, a photoelectrochemical (PEC) cell is used to transform solar energy into solar fuel via a light-activated electrochemical process. In PEC cell solar light is captured either by one or both photoelectrodes together of which at least one is a semiconductor. The working principle of the PEC cell is like PV, where photons with energy equivalent to or higher than the bandgap are required to produce electron and hole pairs and this electrical energy is then used to oxidize/reduce water. In photo-electrolysis solar light absorption capability and water electrolysis are integrated into a single constituent. Photo-electrolysis removes the requirement for a distinct power generator and electrolyzer just like the PV cell and thus PEC cell is more compact [40]. PEC cells can also be used in environmental studies to treat hazardous aqueous waste [72]. As compared to the above-mentioned method PEC is an attractive and promising approach for producing solar H_2. A detailed study about PEC water splitting is addressed in the next section.

1.2 Photoelectrochemical (PEC) Water Splitting

PEC water splitting is an effective, affordable, and carbon-free route to produce H_2 fuel from water utilizing solar energy. The main benefit of this technique is the production of a pure H_2 gas stream that can be employed in a fuel cell [73]. During PEC water splitting sunlight is used to create electron and hole pairs from a photoactive material which is then used to electrolyze water into its constituent H_2 and O_2 in a PEC cell. In short, solar energy is transformed into chemical energy (H_2) by the PEC route [74]. The splitting of water under atmospheric pressure and room temperature is not thermodynamically favorable as it is an uphill reaction (ΔG=237.2 kJ/mol). Water cannot be split directly into its constituents under visible light, only radiations with a wavelength less than 190nm (deep ultraviolet) can split water [75]. Electrochemical splitting of water needs a

The Art of writing only for samples use

least voltage of 1.23V at 298K and neutral pH. Solar irradiance with a wavelength of ~ 1000 nm is found to be equivalent to the minimum required voltage (1.23V) [76]. Thus, if we were able to effectively incorporate solar energy into an electrochemical system dissociation of water can be achieved by using the visible part of the solar spectrum. The idea of PEC water splitting was initially demonstrated by Honda and Fujishima in 1972 by employing titanium dioxide (TiO_2) nanocrystal as photoanode enlightening the potential of solar energy to yield solar H_2 fuel [75].

1.2.1 Concept of PEC Cell Setup

Typical PEC consists of a three-electrode system dipped into an electrolyte aqueous solution, a working electrode that is a photoactive material, a counter electrode of platinum (Pt), and a reference electrode that is a calomel electrode (Ag/AgCl) **(Figure 1.8)**. The working electrode (photoelectrode) is a photoactive light-absorbing semiconductor material with electron and hole pairs formed on its surface when solar irradiance with energy greater than or equal to the semiconductor's bandgap is illuminated. Water is subsequently decomposed into molecular H_2 and O_2 using the photogenerated electrons and holes.

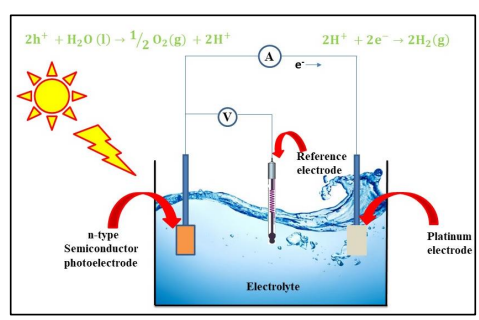

Figure 1.8: Schematic diagram of a PEC cell.

1.2.2 Reaction Mechanism

Water photolysis using PEC water splitting involves several processes at the photoelectrode as well as the photoelectrode-electrolyte interface including

I. Generation of electron-hole pair on the surface of the semiconductor material (photo-anode) under irradiance. Photoexcited electron-hole pairs are isolated from each other by the electric field present at the interface of semiconductors and electrolytes.

$$2h\nu \rightarrow 2e^- + 2h^+ \quad \ldots\ldots (1.1)$$

II. Holes are used for the oxidation of water at the photoanode surface to produce molecular O_2.

$$2h^+ + H_2O\,(l) \rightarrow {}^1/_2\,O_2(g) + 2H^+ \quad \ldots\ldots (1.2)$$

III. Movement of H^+ ion from the photo-anode toward the cathode through electrolyte and movement of photogenerated electron through the external circuit towards the cathode.

IV. Reduction of H^+ ions on the cathode surface by the photoexcited electrons to produce H_2 gas.

$$2H^+ + 2e^- \rightarrow 2H_2(g) \quad \ldots\ldots (1.3)$$

The overall reaction in a PEC water splitting is given by the following equation

$$2h\nu + H_2O\,(l) \rightarrow {}^1/_2\,O_2(g) + H_2(g) \quad \ldots\ldots (1.4)$$

Photoelectrodes used for photoelectrochemical water splitting are divided into two main groups (i) photoanodes and (ii) photocathodes. In general, there are three different ways for the arrangement of photoelectrode inside the PEC assembly.

(i) Photoanode made of n-type semiconductors and cathode made of metal.
(ii) Photocathode made of p-type semiconductor and anode made of metal.
(iii) Photoanode made of n-type semiconductor and photocathode made of p-type semiconductor [77].

1.2.3 Photoanodes

In the PEC system, photoanodes are made up of n-type semiconductors that have been deposited on the surface of a conductive substrate [78, 79]. Under irradiation, the

photoexcited holes in the valence band (VB) are accumulated on the photoanode's surface to carry out the water oxidation reaction. While photoexcited electrons are delivered to the counter electrode through an external circuit and participate in a reduction (red) reaction **(Figure 1.9)**. From an electrochemical viewpoint, the VB edges of the photoanode must be more positive as compared to water oxidation potential **p**ermitting the photoanode to produce O_2 [78]. In simple words quick transfer of hole towards the electrolyte as compared to photo-generated electron leads to anodic photocurrent in PEC water splitting [80, 81].

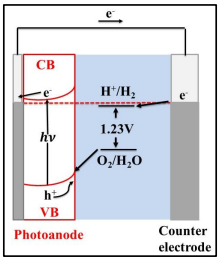

Figure 1.9: Energy diagram of PEC water splitting using n-type semiconductor photoanode. [78]

1.2.4 Photocathodes

Photocathodes consist of p-type semiconductors deposited on a conductive substrate in a PEC setup. As shown in **Figure 1.10** under illumination photoexcited electrons present at the conduction band (CB) of the photocathode possess sufficient energy to reduce water, while oxidation of water happens at the counter electrode. From an electrochemical perspective, the photocathode's CB edge should be more negative as compared to the water reduction potential to produce H_2 [78]. The potential of electrons on the counter electrode is equivalent to the Fermi level (E_f) of the photoelectrode under photoexcitation. If the E_f of the photoelectrode is located at an unfavorable potential, a potential difference may be applied between the working electrode and the counter

electrode to remunerate for the potential shortage and push redox reactions on the counter electrode. Therefore, when photoconversion efficiency is considered, the external power input must be deducted from the total output energy [78, 82]. In other words, the rapid trip of photogenerated electrons to the electrolyte as compared to the hole results in the formation of cathodic photocurrent [80, 81].

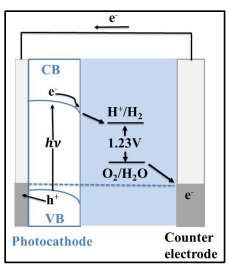

Figure 1.10: Energy diagram of PEC water splitting using p-type semiconductor photocathode. [78]

1.2.5 Unassisted Photoelectrochemical Water Splitting (Dual photoelectrodes)

To overcome the drawbacks of a single photoelectrode-designed PEC cell, like limited absorption over the solar spectrum and water redox overlap, a new method was developed in which two different photosystems are combined in a series for the direct decomposition of water **(Figure 1.11)**. This can be done by the combination of photoanode and photocathode in an arrangement known as a tandem design in which solar light passes through the photoanode first and then through the photocathode. Water is oxidized on the photoanode surface to generate molecular O_2 while reduction occurs on the surface of the photocathode to produce molecular H_2 [83]. In this arrangement, photons from the solar spectrum with shorter wavelengths are collected by the photoanode, while photons with longer wavelengths are absorbed by the photocathode, which results in an enhancement in the consumption of photons by the PEC cell. The photo-voltage of the photoelectrodes is added in such a way to generate enough voltage for splitting water into

its constituents. Secondly, to facilitate the transfer of electrons the photoanode CB edge must be more negative than the photocathode VB edges [84]. Thus in tandem design, the potential required for water splitting is produced directly at the interface (semiconductor-electrolyte) and the energy essential for water splitting is obtained completely from the light source [85].

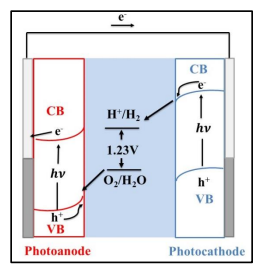

Figure 1.11: Photoanode and photocathode in tandem design. [78]

1.2.6 Requirements of Photoelectrodes

PEC material fabrication aims to design a photoelectrode that must satisfy the following requirement to work efficiently.

(i) The synthesized photoelectrode should be stable in an aqueous solution.
(ii) The as-prepared photoelectrode should be stable against photo corrosion and must show a reversible oxidation state to accommodate photogenerated holes without undergoing decomposition.
(iii) For efficient PEC water splitting the photoelectrode must have a sufficient bandgap (1.6-2.0eV) to harness the maximum portion of the solar spectrum.
(iv) Along with the threshold optical bandgap, the photoelectrode must possess an appropriate electronic band edge position in which the CB lies at a minimum upper than the reduction potential of water, while the VB should lie below the oxidation potential of water. So as the photogenerated electron and hole have sufficient energy for water splitting. Inappropriate bandgap position results in the

need for external biased to create sufficient bandgap bending for water splitting, which reduces the photoconversion efficiency.

(v) The photoelectrode should possess low electrical resistance to facilitate electron transport with a minimum recombination rate [81, 86, 87].

Up to date, not a single material synthesized so far can meet all these criteria. Thus, to attain efficient PEC water splitting, researchers are working on the development of a single photoelectrode that meets all of the above-mentioned requirements.

1.3 Bilayered Photoelectrodes for PEC Water Splitting

Bilayered systems are the most interesting and up-to-date strategies for harvesting a large section of the solar spectrum to improve the PEC performance. Generally, there are two main purposes in the fabrication of bilayered photoelectrodes (i) to have fine control of the interface by using the various synthetic technique, to impart certain useful properties (ii) to enable the photoelectrode to capture a huge part of the solar spectrum.

1.3.1 Mechanism of Bilayered Photoelectrodes

Bilayered photoelectrode consists of two different semiconductors one with a larger bandgap while another one with a smaller/mid bandgap. Bilayered photoelectrode is a multifunctioning material that assimilates different properties of each semiconductor layer. Small bandgap semiconductor is mostly used to sensitize the large band semiconductor by injecting photogenerated electrons or holes after absorbing visible light. For efficient injection of the electron, there should be a proper alignment of CB and VB position of both the semiconductors [81, 88, 89]. Electron transfer between the semiconductors performs a critical part in enhancing the charge transport and reducing the recombination rate by creating a potential gradient at the interface. The semiconductor layers in the bilayered photoelectrode by offering a synergistic effect can cover a wide visible portion of the solar spectrum. The semiconductor present at the top of the bilayered structure usually consists of a large bandgap semiconductor that absorbs a photon of high energy and is transparent to the photon of low energy that is subsequently absorbed by the underlying layer (small/mid bandgap semiconductor) [90].

The Art of writing only for samples use

Thus, the synergistic effect of both layers enhances the photocurrent density as well as improves photoconversion efficiency [91, 92]. The coupling of two different semiconductors possessing different properties can be done in any of the following ways.

1.3.2 n-n junction

In n-n junction, two n-type semiconductors with different properties are coupled together in such a way that the n-type semiconductor thin film of one is deposited over another n-type semiconductor. The CB of the upper semiconductor which is in contact with the electrolyte is more negative as compared to the C.B of the lower semiconductor attached to the substrate, while the VB of the lower layer is more positive as compared to the upper layer. Upon illumination, excitation of electrons occurs from VB into the CB of both semiconductor layers leaving behind holes in the VB. The photoexcited electron moves from the CB of the upper layer (more negative) toward the CB of the lower layer (less negative), while the hole moves oppositely from the VB (more positive) of the lower semiconductor layer into the VB (less positive) of the upper semiconductor layer as **(Figure 1.12 a and b).** As a consequence, the holes are gathered in the VB of the upper semiconductor layer and take part in water oxidation while electrons are accumulated in the CB of the lower semiconductor layer before being transported to the counter electrode and participating in water reduction. [81].

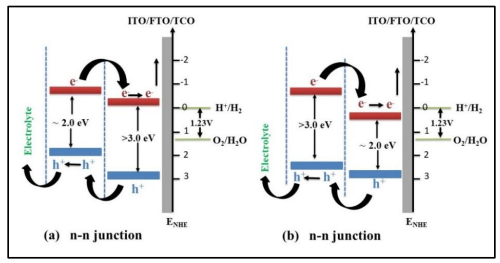

Figure 1.12: Schematic diagram **(a)** and **(b)** for the energy band structure of photoanode forming n-n junction. [81]

The Art of writing only for samples use

1.3.3 p-p junction

This bilayered photoelectrode consists of two different types of p-type semiconductors coupled with each other in such as way having appropriate band edge alignment as revealed in **Figure 1.13**. In p-p junction, the movement of photogenerated electron and holes occur in a direction opposite to the n-n junctions. Photoexcited electrons move towards the semiconductor/electrolyte interface reducing H^+ into H_2 while hole-produced O_2 at the counter electrode [81].

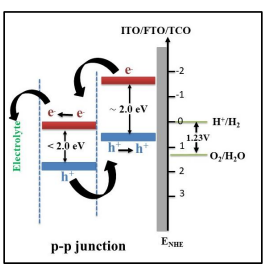

Figure 1.13: Schematic diagram for the energy band structure of photocathode forming a p-p junction. [81]

1.3.4 p-n junction

The p-n junction is bilayered photoelectrodes consisting of n-type and p-type semiconductors coupled together. The p-n junction can behave as photocathodes and photoanode based on the configuration of the semiconductor layers and their band edge positions [93, 94]. The creation of a p–n junction is thought to be a productive technique for increasing electron-hole lifespan, electron-hole separation, and decreasing electron-hole recombination rate. The diffusion of charges produces space–charge region at the electrode junction when a p–n junction is created. [95, 96]. At the heterojunction, an internal electric field is formed by the diffusion of electrons and holes in opposed directions. During irradiation and with the applied bias potential, the as-produced internal electrical

The Art of writing only for samples use

field in a p–n junction can efficiently support charge separation and transfer at the interface, resulting in a high quantum yield [95, 97]. Energetics and electron-hole movement mechanism inside the p-n junction can be seen in **Figures 1.14 (a) and (b).**

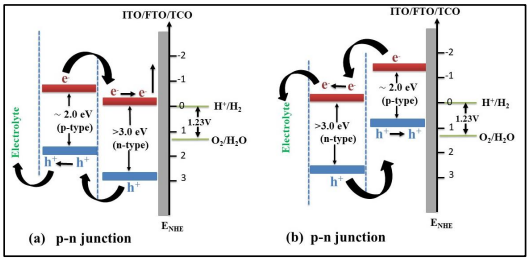

Figure 1.14: Schematic diagram for the energy band structure of photoelectrodes comprising of p-n junction **(a)** photoanode **(b)** photocathode. [81]

1.3.5 Z- Scheme

PEC water splitting can be accomplished *via* a two-steps process, called Z-scheme, by copying natural photosynthesis. In this process, two different kinds of semiconductors are used for photoexcitation and a reversible shuttle redox mediator (donor/acceptor pair). The visible region of the solar spectrum can be more effectively consumed by Z-scheme as compared to the conventional one-step process [98]. In the Z-scheme process, two different semiconductors with incompatible band edges are coupled together through ohmic contact in such a way that the CB and VB of one of the semiconductors are more negative as compared to the second one [99]. Ohmic contact in Z-scheme triggers the recombination of photoinduced electrons and holes with lower reduction and oxidation potential, leaving behind electrons and holes with higher reduction and oxidation potential and thereby providing high redox potential to visible light active short band-gap semiconductor systems [100]. The schematic illustration of electron flow through the Z-scheme can be seen in **Figure 1.15**.

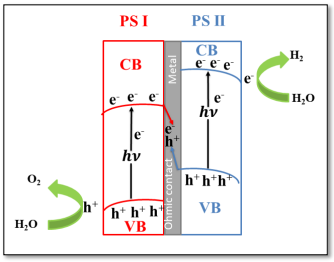

Figure 1.15: Schematic illustration of PEC water splitting, charge transfer with Z-scheme configuration. [101]

1.3.6 Advantages of Bilayered Films over the Single-Layered Film.

The advantage of Bilayered films over a single-layered film in terms of photocurrent density and photoconversion efficiency can be credited to the below-mentioned reasons.

(i) The coupling of large bandgap semiconductors with small band semiconductors plays a significant part in shifting the absorbance of the photosystem toward the visible region of the solar spectrum.

(ii) Improve charge separation in both semiconductors, resulting in less photogenerated electron and hole recombination.

(iii) The charge carrier's lifespan is extended [81].

1.4 Fabrication of Photoelectrodes

Selecting an ideal fabrication method for PEC water splitting depends on multiple factors such as the size of the photoelectrode, shape complexity, production amount, financing, energy requirement, etc. A trilateral closed-loop connection exists between material, properties, and manufacturing process. The bulk and surface properties of synthesized photoelectrode are found to be dependent on the synthetic approach and conditions. The synthetic methods used to produce photoelectrodes are largely divided into two divisions physical methods and chemical methods.

1.4.1 Physical Method

Physical deposition methods are based on physical phenomena that are used to form and deposit the requisite material on the substrate. Physical methods are categorized as liquid phase precursor methods or vapor phase precursor methods depending on the precursor phase.

1.4.2 Liquid-phase Precursors Methods

In the liquid phase precursor methods, precursors utilized are in the liquid phase. Subsequent chemical reactions like precipitation or hydrolysis reactions are used to coat nanomaterials on the required substrate. Numerous techniques that can be applied in the liquid phase precursor method are described below.

1.4.2.1 Dip Coating

Among various techniques used for photoelectrode fabrication, dip coating is a simple and possibly the earliest method used for coating purposes [102]. In principle, a stable solution of the nanomaterial which has to be deposited is prepared in a volatile solution. A clean substrate is then dipped into the prepared solution at a steady speed for the required interval. After that, the photoelectrode is then taken out and dried to vaporize the solvent. Dip coating produces an even and uniform thin coat of nanomaterial over the substrate. Dip-coating may be (i) batch type dip-coating or (ii) continue type dip-coating. Both kinds of dip-coating include the following common steps, immersion, start-up, deposition, drainage, and evaporation.

Yin *et al.* developed $ZnFe_2O_3/TiO_2$ double-layered film photoelectrode on indium tin oxide (ITO) by using the dip-coating method. PEC studies confirm that the photocurrent density (J_{sc}) of $ZnFe_2O_3/TiO_2$ doubled film initially increases and then decreases with an increase in thickness $ZnFe_2O_3$ layer. An uppermost J_{sc} of $0.1\ mA/cm^2$ was acquired when the TiO_2 nanoparticle was covered with 2-times $ZnFe_2O_3$ which is a 5-fold increment in J_{sc} in comparison to bare TiO_2 film ($0.02\ mA/cm^2$). This improvement in the J_{sc} is credited to the shift of TiO_2 photoresponse towards the visible region upon deposition of $ZnFe_2O_3$ [103]. Maabong *et al.* fabricate Ti-doped hematite (α-

Fe_2O_3) thin film on FTO by coating iron oleate sol-gel using a dip-coating technique continued by drying over the hot plate at 70°C before annealing at 550 °C (10°C/min) for a period of 0.5h. PEC measurements show that α-Fe_2O_3 thin film doped with 1wt% Ti shows an utmost J_{sc} of $0.72\ mA/cm^2$ at1.23V_{RHE} that is 2 times better than pure α-Fe_2O_3 film ($0.30\ mA/cm^2$ at1.23V_{RHE}) [104].

1.4.2.2 Spin Coating

The spin coating strategy employs centrifugal force to coat the appropriate material on the desired substrate [105]. Normally, a clean substrate is put on a spin coating machine chunk (**Figure 1.16**). To fix the substrate in a particular position, a vacuum is created underneath it and then rotated at a very high speed. The nanomaterial suspension or solution is then dropped slowly onto the substrate due to centrifugal force the suspension spread to the edges and completely covers it. The thickness of the coating decreases with an increase in angular speed [106]. The substrate is then leftover for solvent evaporation leaving behind a thin film of required material.

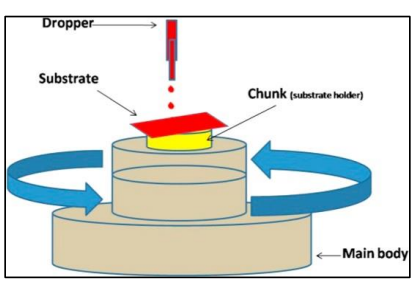

Figure 1.16: Schematic diagram of a spin coating method. [107]

Zhang *et al.* deposited ultra-thin film of α-Fe_2O_3 over the TiO_2 underlayer and employed it as a photoanode for PEC water splitting. TiO_2 underlayer was layered over FTO substrate by spin coating technique using TiO_2 nanoparticles having particle size 15-

20 nm dissolved in ethanol while the α-Fe_2O_3 ultrathin film was deposited over the TiO_2 underlayer by a two-phase hydrolysis-solvothermal reaction. The apparent improvement of the PEC efficiency by the TiO_2 under layer was credited to the lessening of the dead layer effect and improved surface area for deposition of sufficient α-Fe_2O_3 to expand light absorption capability. It was reported that α-Fe_2O_3 thin film must be thin enough to efficiently reduce the charge recombination and thick enough to efficiently consume photon energy. Optimized photoanode shows a maximum J_{sc} of $0.683 mA/cm^2$ and an IPCE value of 19.8% at 1.5V_{RHE} [108]**.** Emin *et al.* synthesized porous α-Fe_2O_3 thin films on FTO substrate by spin coating colloidal core/shell Fe/Fe-oxide nanoparticles. The as-developed α-Fe_2O_3 thin films were used as photoanode for water oxidation measurements after calcination in air at various temperatures (800°C, 700°C, and 600°C). The main advantages of employing Fe /Fe-oxide nanoparticles are that they produce a firm suspension in an organic solvent that is convenient for spin coating. PEC measurements show that 300 nm thin α-Fe_2O_3 film annealed at 800°C displays the uppermost J_{sc} of $0.75\ mA/cm^2$ at 1.23V_{RHE} [109]**.**

1.4.2.3 Doctor Blade Printing

Doctor blade printing, also known as tape casting, is the utmost popular coating method for lab-scale dye-sensitized solar cell (DSSC) fabrication, owing to its economical nature, user-friendliness, and lack of moveable components [110]. It can also be used by amateurs due to its easiness and economical nature. The device consists of a substrate holding stage, a sharp moveable blade, and a few fixtures **(Figure 1.17)**. The substrate is positioned on the stage, and the blade is placed over the substrate with the proper space among the blades, which determines the coating thickness. A paste containing the appropriate nanoparticles is applied to the desired substrate and dispersed uniformly with a sharp blade. This procedure was frequently repeated to enhance the thickness or to create a multilayer structure. After a steady coating, the substrate is eventually detached from the stage and placed for drying.

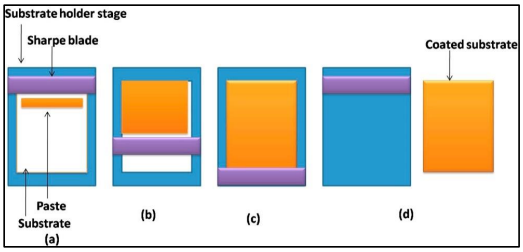

Figure 1.17: Schematic diagram (top view) of a doctor blade technique. [107]

Rani *et al.* synthesized ultra-fine Metal (M) doped TiO_2 nanospheres (M=Fe, Ce, and La) by using a low-temperature solvothermal approach. The doctor blade technique was employed to deposit the synthesized Fe, Ce, and La doped TiO_2 nanospheres on the FTO substrate. PEC measurements show that the foreign cation doped TiO_2 nanosphere shows high PEC activity as compared to pristine TiO_2 photoelectrode without bias. It was reported among all the dopant 10% La-doped TiO_2 photoelectrode shows uppermost J_{sc} of $0.48\ mA/cm^2$ that is twice greater than bare TiO_2 photoanode. The up-gradation in the J_{sc} has been credited to the synergetic effect of nanospheres, optimum bandgap, better charge separation, low recombination rate, and enhanced light absorption spectral range. [111]. Liu *et al.* used a combination of laser ablation in liquid and a hydrothermal method to make Ge-doped α-Fe_2O_3 nanocrystals with numerous doping concentrations. The doctor blade technique was employed to deposit the synthesized Ge doped α-Fe_2O_3 nanocrystal on the FTO substrate. It was reported that by changing the ablation period, the Ge doping level and α-Fe_2O_3 morphology can be easily adjusted. The distribution of dopant Ge was found to be affected by the dopant level. At a low doping level (2%), Ge dopants randomly substituted Fe sites resulting in the formation of ultra-thin circular morphology having a diameter of 200 nm and a thickness of 100 nm. However, when the Ge level was high (5%) the dopants underwent chemical ordering, resulting in the doubling of the basal vectors and the formation of a superlattice structure owing to nanosheets morphology having 30-40 nm thickness. PEC studies 2% Ge doped α-Fe_2O_3 photoanode shows

uttermost J_{sc} of $105\ \mu A/cm^2$ at 0.23 $V_{Ag/AgCl}$, followed by 5% Ge doped α-Fe_2O_3 ($28\ \mu A/cm^2$ at 0.23 $V_{Ag/AgCl}$) and pristine α-Fe_2O_3 ($11\ \mu A/cm^2$ at 0.23 $V_{Ag/AgCl}$). Enhancement of J_{sc} was credited to the lowering in band-gap of α-Fe_2O_3 due to Ge doping [112].

1.4.2.4 Electrospray Deposition (ESD)

ESD is based on the electrostatic painting process, which involves atomizing paint particles and directing the flux toward the grounded portion of the required surface to be painted. However, in the ESD process charged particles of solution are sprayed on an already prepared grounded substrate, resulting in a uniform layer on the substrate [113].

A pump is used to pressurize the solution, a nozzle to atomize the droplets and to charge the atomized droplet a power supply makes up an ESD apparatus, as shown in **Figure 1. 18**. These charged droplets are then guided and deposited on an already grounded substrate. The key benefits are that this approach uses fewer nanoparticles and has a waste rate of just 5-8 %.

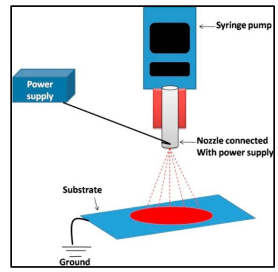

Figure 1.18: Schematic diagram of an ESD method. [107]

Rahman *et al.* synthesize α-Fe_2O_3 thin film on the FTO by using the ESD technique and employed it as a photoanode in PEC studies. The impact of synthesis

parameters like discharge potential, the temperature of the substrate, and post-heat treatment on the morphology, grain size, and PEC performances of α-Fe_2O_3 thin films were explored. It was found that the surface morphology of the as-prepared α-Fe_2O_3 film changed from a packed worm-like surface to highly porous nanostructures as the substrate temperature increased. By varying the discharge potential, a reduction in the size of the nanoparticle was noticed. PEC measurements show under optimized condition nanostructure α-Fe_2O_3 thin film photoelectrode show maximum J_{sc} of $0.6\ mA/cm^2$ at 1.23 $V_{Ag/AgCl}$ and an IPCE value of 13% at 350 nm [114]. Yoon *et al*. successfully synthesized WO_3 thin film photoelectrode on ITO glass substrate for PEC water splitting by using the ESD technique. To create a connection between film thickness and water splitting efficiency, the thickness of the films was altered from 50 to 400 nm. Photoresponse of the as-prepared WO_3 thin film was found to be increased with an upsurge in the thickness of the film. PEC measurement reveals that the J_{sc} of WO_3 film electro sprayed for 10 min (90 nm thick) was $0.04\ mA/cm^2$ and is significantly increased 10 times **(**$0.40\ mA/cm^2$) when the electro sprayed deposition period was prolonged to 60 min (400 nm). This betterment in the PEC performance is credited to the increase in the bulk volume of WO_3 by increasing the deposition time and therefore provides more site for the generation of charge carriers upon illumination [115].

1.4.3 Gas-phase Precursors

In the gas-phase precursor methods, the precursors used are in the gaseous phase (atom diffuse broadly in gas). The coating is performed by ionizing the gas atoms to deposit the required nanomaterials on the substrate. Some of the techniques utilized in the gas phase precursor method are described below.

1.4.3.1 Physical Vapor Deposition (PVD)

In PVD development of films happens due to the condensation of atoms on a low-temperature substrate. The primary step in PVD is vaporization of the material to be deposited, its transportation to the substrate followed by condensation and nucleation of adsorbed atoms on the substrate surface. PVD can be classified into two types depending

on the evaporation methods used in the process: thermal and non-thermal (sputtering) evaporation [107].

1.4.3.1.1 Thermal Evaporation

Thermal evaporation uses heat energy to trigger the deposition process proceeded by substrate cleaning and etching if required. The evaporation source may be electron beam heating, a resistive heating source, an inductive heating source, or an electrically heated crucible holding the material to be evaporated [107]. The rate of evaporation is mainly calculated by the source material's vapor pressure at the evaporation temperature. To prevent oxidation of the source a highly vacuumed ($< 10^{-2}$Pa) deposition chamber is much necessary. To avoid the destructive reaction between the crucible and the source rapid heating is needed, which is referred to as flash evaporation. If the deposited film is thermally or flash evaporated, the characteristics of the coated film are found to be dissimilar [116]. Some of the main drawbacks associated with thermal evaporation are (i) poor adhesion due to low affinity as a result an adhesive layer is required (ii) metal and low melting material can be easily deposited, however, for refractory and multicomponent material thermal evaporation is not that much useful (iii) contamination problem and poor step coverage [117].

Thermal evaporation of highly sensitive material under ultra-high vacuum (UHV)10^{-6}Pa is obtained by using an electron beam evaporator. In an electron beam evaporator, high-speed electrons are used to bombard the source material. The kinetic energy is transformed into thermal energy in this process, which raises the temperature of the source. One of the main advantages of using an electron beam evaporator is that contamination from the crucible is prevented and a high temperature is reachable. Thermionic emission or field-effect cathodes are used to produce electron beams. [116]. Electron beam evaporation is found to be very useful in enhancing the thickness of deposition uniformly and creating multiple layer deposition simply by exchanging the crucible and assembling several possible target films. However, the main issues related to this method are the enormous use of electricity and X-ray [117]. **Figure 1.19** shows a schematic diagram of the thermal evaporator and electron beam evaporator [117].

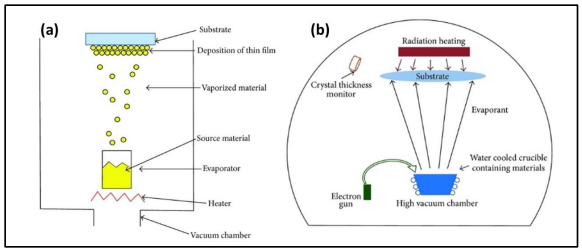

Figure 1.19: Schematic diagram of **(a)** thermal evaporator **(b)** electron beam evaporator. [117]

1.4.3.1.2 Sputter Deposition

Sputtering is a non-thermal method in which bombarding species of molecular or atomic size physically eject the surface atom of the target material by momentum transfer. In sputtering generally an ion beam or flux of ions created by using electrical energy is bombarded on the target material **(Figure 1.20)**. By transferring momentum, these incident ions make atoms or clusters of atoms to be expelled from the desired surface. Sputtering etching and sputtering depositions are the two main applications of the sputtering process. Sputtering is classified into different types based on the source and method used to eliminate atoms from the target surface, such as radio-frequency (RF) sputtering, diode sputtering, magnetron sputtering, triode sputtering, arc deposition, and pulsed laser deposition [107].

Leroy *et al*. synthesized $LaTiO_2N$ photoelectrode decorated with an In_2O_3 overlayer by using radio-frequency (RF) sputtering. It was reported that deposition of In_2O_3 overlayer enhances the photocurrent by 2-3 times. PEC measurement shows that $LaTiO_2N/In_2O_3$ photoelectrode shows an optimum J_{sc} of $0.61\ mA/cm^2$ at $1.23V_{RHE,}$ in comparison to the bare $LaTiO_2N$ photoelectrode **(**$0.24\ mA/cm^2$ at $1.23V_{RHE}$). This improvement in PEC activity is credited to (i) effective charge separation and reduced charge recombination owing to the suitable CB and VB position of the semiconductor

used (ii) improved charge separation due to the surface dipole created among $LaTiO_2N/In_2O_3$ [118].

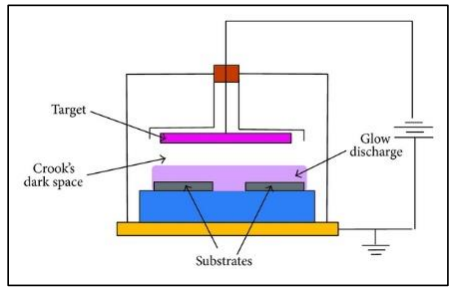

Figure 1.20: Schematic diagram of diode sputtering deposition. [117]

Lai *et al*. fabricated TiO_2 nanotube (NTs) photoelectrode decorated with WO_3 using RF sputtering to improve its PEC performance. It was recorded that an enhancement in the J_{sc} and photoconversion can be achieved if the WO_3 layer thickness and distribution are precisely monitored. Loading of W in a minute amount (RF sputtering for 0.5 min) leads to the integration of W ion (W^{6+}) into the TiO_2 lattice that effectively separates the electron/hole pair, and an improvement in the PEC performance was observed. However, too much W loading leads to the formation and accumulation of WO_3 over the top part of TiO_2NTs instead of incorporating into the lattice, which acts as recombination canters, and a lower PEC response was observed. A maximum J_{sc} of $1.6\ mA/cm^2$ with a photoconversion efficiency of 2.65% was observed for WO_3-TiO_2 NTs hybrid deposited for a while of 0.5 min. This enhancement in the J_{sc} is assigned to the quick transport of photoexcited electrons and holes preventing their backward reaction and decreasing the recombination sites [119].

Fernandes *et al*. fabricated TiO_2 nanotube arrays (NTAs) sensitized with CdSe (TiO_2/CdSe) through RF magnetron sputtering for different periods and employed them

as photoanodes for PEC studies. To obtain a better TiO_2/CdSe interface the synthesized TiO_2/CdSe photoanodes were calcined at various temperatures. The PEC measurement shows that among all the photoelectrode TiO_2/CdSe_30/40 photoelectrode (RF magnetron sputtering for 30 minutes and calcined at 400°C) display the uppermost J_{sc} of $1.9\ mA/cm^2$ at 0.6 $V_{Ag/AgCl}$ which is 5 and 535 times greater than that shown by pure TiO_2 under 1sun and visible light irradiance [120].

1.4.4 Chemical Methods

Chemical methods of deposition depend on chemical reactions between substrate-precursor and precursor-other chemical medium to prepare and deposit nanomaterial on the substrate surface. The chemical method is widely categorized as liquid phase deposition and vapor phase deposition depending on the precursor phase.

1.4.4.1 Liquid-phase Precursor Methods

In these methods, the precursors involved are in the liquid phase. Numerous chemical reactions like hydrolysis and precipitation are used for deposition. Various techniques used in the liquid precursor method are as follows.

1.4.4.1.1 Hydrothermal/Solvothermal (HT/ST) Methods

HT/ST methods are mostly employed to produce single crystal and nanostructure of numerous semiconductor oxides and other materials. The principal difference between the solvothermal and hydrothermal processes is that in the solvothermal approach water is not used as a solvent preventing species oxidation. HT/ST methods provide definite control over surface morphology, particle size, distribution, and shape of the synthesized crystal. German geologist Karl Emil von Schafhäutl announced the first one to report hydrothermal crystal growth in 1845 when he developed microscopic quartz crystals inside a pressure cooker. Under high temperature and pressure inside an autoclave soluble metal salts dissolved in an aqueous or organic solvent or a combination of both are reacted. Crystal nucleation occurs on the surface of the substrate (with or without seeds) and subsequently directed growth leads to crystal alignment on the required substrate [121]. HT/ST methods use simple equipment like an autoclave**, (Figure 1.21)**

that's why they are favoured over other sophisticated deposition techniques safety hazards related to chemical reagents and the lack of see-through windows in autoclaves apparatus are among the drawbacks.

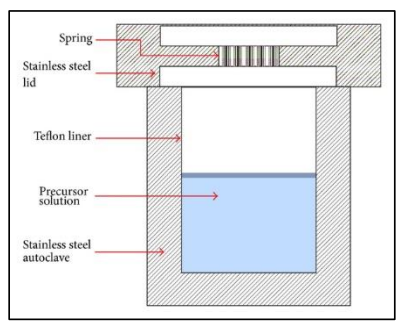

Figure 1.21: Schematic diagram of autoclave used in HT/ST methods.

Xu *et al*. used a one-pot hydrothermal approach to integrate Sn into the TiO_2 nanowire array by varying $SnCl_4$, and tetrabutyl titanate ratio. The doping level of Sn was kept restricted at a very minor level that is 1-2% (Sn/Ti molar ratio) to evade interface scattering or phase separation. PEC studies show that the J_{sc} upsurges with an increase in Sn doping amount and spiked at $> 2.0\ mA/cm^2$ at 0 V $_{Ag/AgCl}$, which is twice that of bare TiO_2 photoanode. However, an additional increase in Sn doping results in a decrease in J_{sc} and finally reaches or drops to the value of bare TiO_2 may be due to phase separation and upshift of TiO_2 bandgap [122].

Annamalai *et al*. fabricated Sn doped α-Fe_2O_3 photoelectrode using a hydrothermal approach for enhanced PEC water oxidation studies. Doping of Sn was done both by *in-situ* as well as *ex-situ* methods. *In-situ* doping was done by adding the required quantity of $SnCl_4$-ethanol solution to the hydrothermal precursor solution. However, *ex-situ* doping was done by dipping bare α-Fe_2O_3 photoelectrode into $SnCl_4$

precursor solution and then annealing at 800 °C. It was reported that in-situ doping of Sn leads to the creation of Sn-doped α-Fe_2O_3 with nanocorals morphology with (104) plane as the dominant direction of crystal growth, however, ex-situ doping keeps preserve the vertically aligned nanorod morphology and keeps the orientation of (110) plane, which is very much suitable for high conductivity in pristine α-Fe_2O_3. PEC measurements at 1.4V_{RHE} show that *ex-situ* doping results in a 60% upsurge in the J_{sc} while *in-situ* doping gives a 20% increment in the J_{sc} compared to bare α-Fe_2O_3. This enhancement on the J_{sc} is credited to the Sn doping that works as an electron donor by enhancing the charge density, and also delivering superior surface charge transfer kinetics, hence boosting the system's overall performance [123].

Yang *et al.* use a seed layer-free route to synthesize a smooth $WO_3.H_2O$ plate-like array on FTO substrate using a hydrothermal approach under mild temperature with the help of ammonium oxalate as a structural directing agent. The crystal structure and morphology of the synthesized photoelectrode were found to be greatly influenced by the hydrothermal temperature and reaction time. XRD data reveal that the $WO_3.H_2O$ thin films synthesized at a temperature below 150°C were orthorhombic and were wholly transformed into monoclinic at 180°C. Morphological studies reveal that the thickness of the plates was found to increase with an increase in reaction temperature and growth period. The plate-like $WO_3.H_2O$ morphology was completely converted into an irregular block as the growth/reaction temperature was exceeded above 180°C. It was also found that ammonium oxalate also shows a significant part in the growth of the vertically arranged plate-like array. Furthermore, PEC measurements show that the dehydrated WO_3 plate annealed at 450 °C shows improved and stable photocatalytic activity for water splitting. It was reported that among all the photoelectrode plate-like arrays produced at 120°C for 12 h displays the uppermost anodic photocurrent of 4.13 mA/cm^2 at 1.6 V_{Ag}/AgCl under 500W Xe lamp illumination in 0.5M H_2S0_4 electrolyte [124].

1.4.4.1.2. Chemical Bath Deposition (CBD)

CBD has gotten major attention as it does not require any complicated or costly equipment such as a vacuum system. Chemical bath deposition simply contains a precursor solution container provided with a stirring and heating system along with a fixture to hold the substrate as depicted in **Figure 1.22**. With the CBD system by using a proper jig design we can easily coat many substrates with a single run. Electrical conductivity of substrate is not that much required in CBD deposition, any insoluble substrate to which the solution has easy excess can be used. However, in low-temperature CBD deposition oxidation corrosion of metallic substrate can be avoided. With CBD deposition we can simply regulate the film thickness, size, shape, and morphology of the deposited material by varying deposition time and deposition temperature. Simply CBD method can be highly useful in synthesizing uniform, stable, and adherent films with good reproducibility [107].

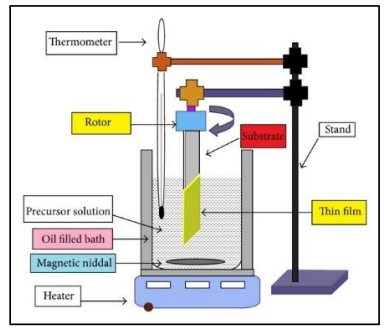

Figure 1.22: Schematic deposition method using CBD [125].

Hoang *et al.* grows vertically aligned TiO_2 nanoplatelet arrays on FTO substrate by CBD method and used them for PEC and DSSC applications. The TiO_2 arrays possess a single crystal rutile phase TiO_2 nanoplatelet having a length of up to 130 nm, a width of

~ 5 nm, and height (film thickness) up to 1μm. The growth of TiO_2 nanoplatelet was discovered to be greatly influenced by acidity and precursor concentration ($TiCl_3$). It was assumed that regulating the hydrolysis and oxidation of Ti^{3+} using a minute concentration of $TiCl_3$ (8-40 mM) and low pH (0.71-0.85) is the main step to obtain a nanoplatelet framework. PEC studies show that for water oxidation the synthesized TiO_2 nanoplatelet array photoelectrode shows a maximum J_{sc} of 0.6 mA/cm^2 at very low bias potential of ~0.6 $V_{Ag/AgCl}$. However, DSSC fabricated using N719 dye and TiO_2 nanoplatelet array also display encouraging results with photoconversion efficiency of 1.28% for as-prepared TiO_2 nanoplatelet and 3.7 % for annealed TiO_2 nanoplatelet [126].

Rahman *et al.* fabricate nanosized α-Fe_2O_3 on an FTO substrate by using a facile and cost-effective CBD approach. Morphological, structural, and optical properties of the as-synthesized α-Fe_2O_3 were tuned by differing experiment variables such as deposition temperature and precursor concentration. The surface morphology of the α-Fe_2O_3 was found to vary from granulated shaped condensed particle to allied rod-like structure by changing Fe precursor concentration from 0.1 to 0.3 M. By varying the deposition temperature from 60 to 90 °C an increase in the particle size was observed, while morphology remains unchanged. PEC measurement shows that optimized α-Fe_2O_3 photoelectrode shows a maximum J_{sc} of 700 $\mu A/cm^2$ at 1.6 V_{RHE} under 1 sunlight radiance (AM 1.5) in 1M NaOH [127].

1.4.4.1.3. Electrochemical Deposition

Electrochemical techniques are not only used as capable analytical methods to evaluate the performance of electrode material but can also provide an efficient synthetic approach for preparing various electrodes [128, 129]. Using the electrochemical method, a wide range of metals, metal oxides, semiconductors, ceramic materials, conducting polymers and thin films of required thickness can be deposited on a conductive substrate [130-133]. Electrochemical deposition comprises electro-deposition, electrophoretic deposition, and electroless deposition. In electro-deposition, electric current is delivered to electrodes that are submerged in an appropriate electrolyte holding ions of the deposited species [107]. The loading of active material on the conducting substrate was found to be greatly affected by

certain electrodeposition parameters such as deposition charge density, deposition time, applied potential, and precursor concentration [134]. These parameters are found to be very critical and allow a high control over the final morphology of the electrode. For example, potential applied on the electrode directly affects the pace at which electrons are produced along with nucleation and crystal growth [135]. The possibility of carrying out electro-deposition under ambient temperature and pressure makes the electro-deposition an easy, simple, and cost-effective method.

Electroless deposition is an auto-catalytic chemical method for depositing ionic species present in the electrolyte on the appropriate substrate, in the absence of electric current. The electroless deposition is generally carried out in the existence of a reducing agent that chemically reacts with ions to get deposited [107]. Electrophoretic deposition is a multifunction technique that is broadly employed in DSSC, lithium-ion batteries, supercapacitors, fuel cells, and light-emitting diodes due to its low cost, small deposition time, and electric controllability [136-140]. Electrophoretic deposition is dependent on the drive of charged particles inside a stable suspension and gets deposited steadily onto the surface of the substrate forming an evenly deposited film by the application of an applied electric field [141, 142]. One of the main advantages of the electrophoretic deposition method is that it provides control of the shape, composition, and thickness of the deposited films by varying applied electric field, deposition period, and concentration of the suspension [143, 144].

Li *et al.* successfully synthesized phosphorus cation doped TiO_2 nanotube photonic crystal (P-TiO_2 NTPC) by using a two-step electrochemical anodization approach followed by phosphidation. P cation doping scheme was employed to uplift PEC activity of P-TiO_2 NTPC in both visible lights as well as under full sun-light illumination. P cation (P^{5+}) partially replaces Ti^{4+} in the crystal lattice, which causes a lowering in the TiO_2 bandgap and induces charge imbalance owing to the creation of a Ti-O-P bond. PEC measurements show that the P-TiO_2 NTPC photoanode shows an optimum J_{sc} of 0.78 mA/cm^2 at 1.23V_{RHE} is almost 140% greater than pure TiO_2 NTPC (0.32 mA/cm^2 at 1.23V_{RHE}) [145].

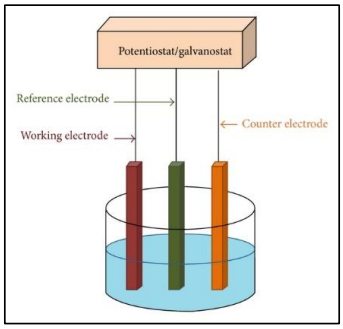

Figure 1.23: Schematic representation of electrochemical deposition. [125]

Nasiri *et al*. synthesized α-Fe_2O_3/reduced graphene oxide (α-Fe_2O_3/rGO) nanocomposites photoanodes on FTO substrate by using the electrochemical deposition technique and the impact of annealing temperature (300, 500, and 700°C under N_2 atmosphere) on PEC activity was investigated. PEC results show that α-Fe_2O_3 /rGO nanocomposite shows a high J_{sc} as compared to pristine α-Fe_2O_3. It was reported that the interaction between the oxide group of rGO and α-Fe_2O_3 increases the photogenerated electron conductivity and lessens the recombination pace of the electron/hole pair which results in improvement of PEC activities. Among all the photoanode α-Fe_2O_3 /rGO nanocomposite annealed at 700 °C shows the uppermost J_{sc} of $0.98\ mA/cm^2$ that is 88% greater than pure α-Fe_2O_3 ($0.1 mA/cm^2$) [146].

Tezcan *et al.* prepared ZnO nanorod arrays on ITO substrate using the electrochemical deposition method at various deposition potentials (-0.7, -0.8, and -0.9 V) under constant pH (~6) and temperature (70°C) for 30 min each. The effect of deposition potential on their morphology, optical properties, and PEC performance was investigated. Morphologically studies reveal that the thickness of the nanorod array was greatly affected and can be altered by varying the deposition potential. PEC measurement

shows that all the synthesized ZnO photoanode synthesized at -0.8 V show maximum photoconversion efficiency of ~0.15 % followed by -0.9 V (~0.65%) and -0.7 V (~0.4 %) [147].

Deng *et al*. effectively produced a hierarchal 3D TiO_2/Fe_2O_3 heterojunction *via an* electrophoretic deposition technique that results in an improved PEC activity. PEC measurements show that TiO_2/Fe_2O_3 photoanode have an optimum J_{sc} of $1.79\ mA/cm^2$ at $1.23V_{RHE}$ almost 2.1 times greater than pure Fe_2O_3. Depending on XPS and EIS results the improved PEC activity was credited to the effective separation and transmission of photoexcited charge carriers in TiO_2/Fe_2O_3 heterojunction [148].

1.4.4.1.4. Spray Pyrolysis (SP)

After the inventive work done by Chamberlin and Skarman in 1966 to prepare CdS for solar cells, SP has been used for the last three decades to grow an extensive range of materials in the forms of thin films [149]. Due to the simplicity of the apparatus, low cost, least waste production, and good productivity over a large scale, SP is the most useful technique to prepare thin films of noble metals, chalcogenides (quaternary, ternary, and binary), metal oxides, spinel oxides, and superconducting compounds. Optimization of deposition parameters like spray rate, substrate temperature, and concentration of the solution is highly essential for obtaining high-quality thin films. However, in recent few years, the selection of atomization techniques like electrostatic SP, corona SP, ultrasonic nebulization, and micro spray-based SP has received serious interest. It is one of the most important parameters as it enables control of droplet size and its spreading over the preheated substrate. Despite its simplicity, the spray pyrolysis method has also some serious advantages: (i) with SP one can easily dope films with any element in any quantity and form by simply incorporating it into the spray solution. (ii) contrary to the closed vapor deposition techniques SP can be used on an industrial scale since it doesn't require any high-quality target/substrate nor does it need any vacuum system at any step (iii) deposition pace and thickness of the film can be simply monitored by altering the spray parameters which give it advantageous over traditional method like the sol-gel method that produces films of a limited thickness (iv) SP can also be operated at low

temperature (100-500 °C) to prepare films over fewer robust materials (v) dissimilar to high-power techniques like radio frequency magnetron sputtering (RFMS) it does not produce local overheating that is dangerous to the material to be layered/deposit. Secondly, there are not so many restrictions on the substrate material type, size, or surface profile (vi) Using SP one can make layered film or film with composition gradient across the thickness by simply varying the composition of the spray solution throughout the spray phase [150]. A diagrammatical representation of the SP method is revealed in **Figure 1.24.**

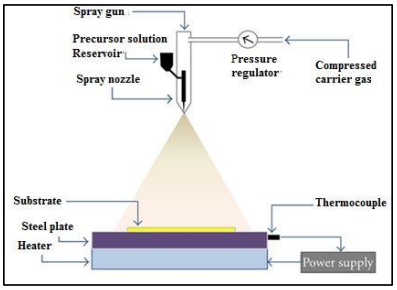

Figure 1.24: Schematic diagram of spray pyrolysis method. [151]

Ranasinghe *et al*. produced robust and highly active thin films of TiO_2 on FTO through atomized spray pyrolysis deposition (ASPD) and applied it as a photoanode in PEC studies. PEC performance of optimized TiO_2 thin film shows a J_{sc} of $\sim 5\ mA/cm^2$ at 1.0 V under 375 nm ($150\ mW/cm^2$) and an IPCE value of 14% that is twice greater than the photoelectrode synthesized by traditional SP deposition over the same substrate temperature and precursor concentration. The higher PEC activity and stability shown by photoanode synthesized by ASPD are attributed to the greater crystallinity and excellent charge conductivity. On the other hand TiO_2, photoelectrodes synthesized from TiO_2 powder by conventional SP deposition possess high defects derived from the grain boundaries and junctions amongst the particles that deeply trap electrons [152].

Hussain *et al.* synthesized $ZnFe_2O_4/Fe_2O_3$ composite thin film with the various molar ratio on a 3-D nano spikes substrate for PEC water oxidation using spray pyrolysis deposition. PEC studies show that $ZnFe_2O_4/Fe_2O_3$ synthesized with a 1:1 molar ratio shows the utmost J_{sc} of $2.19\ mA/cm^2$ for PEC water oxidation that is 3.4 and 2.73 times greater than the J_{sc} shown by bare α-Fe_2O_3 on plane FTO, and so for the maximum recorded J_{sc} value for such photoelectrode. In summary, the highest PEC performance of as-prepared $ZnFe_2O_4/Fe_2O_3$ photoanode was attributed to the prominent charged mobility throughout the possible interfaces (FTO/semiconductor/electrolyte), a nanostructured substrate that shows effective charge separation and improved optical absorption [153].

Aboud *et al.* explored the effect of metallic doping (Pb, Cu, and Ni) on the PEC activity of ZnO thin films produced by SP deposition under the same doping level (3 wt %). All the synthesized photoanodes possess the same particle size of 50 nm. PEC studies show that among all the synthesized photoanode Pb doped ZnO shows the uppermost J_{sc} with IPCE and ABPE value of ~30% at 390 nm and 0.636 at 0.5 V, correspondingly [154].

1.4.4.1.5. Sol-gel Coating Method

The sol-gel method has come into existence as long since the mid-1800s [155]. The sol-gel technique has been utilized in the production of novel materials for catalysis, chemical sensors, membranes, photochromic applications, fibers, optical gain media, solid-state electrochemical equipment, and in a variety of other science and engineering fields, including nuclear, ceramic, and electronic industries [155-163]. Sol-gel is among the topmost studied coating techniques and is mostly practiced in developing thin film and powder catalysts. Literature study reveals that the sol-gel technique has gone under many modifications to develop pure thin films along with powders in huge homogenous concentrations under constant stoichiometry check [164, 165]. The sol-gel method is also known as molecular level mixing and is mostly used to form finer size metal oxide particles. The sol-gel technique begins with the preparation of a colloidal solution (sol), which is then turned into a gel, which is subsequently dried and crushed into nanosized oxide particles [166]. The gel can also be layered straight on the desired substrate and dried

to develop fine coated films. The sol-gel technique can also be used to produce doped nanoparticles as well as composites. One of the main benefits of photoelectrode synthesized by the sol-gel method is its effective charge separation capability, and proper surface properties [167].

Liu *et al.* used sol-gel to develop mesoporous TiO_2/WO_3 nano honeycomb photoelectrode with a molar ratio of 3.1 for PEC water splitting studies. To enhance the porosity the composite TiO_2/WO_3 was deposited with an internal template of block copolymer over a substrate layered with nanospheres of polystyrene (PS). The final mesoporous TiO_2/WO_3 photoelectrode was obtained after removing the PS nanosphere and block copolymer by thermal treatment. The synthesized mesoporous TiO_2/WO_3 honeycomb photoelectrode show an uttermost J_{sc} of $0.4\ mA/cm^2$ at +0.4 V_{SCE} which is almost twice higher than for the solid TiO_2/WO_3 photoelectrode synthesized in the absence of a block copolymer template. The enhancement in the photocurrent of the as-prepared mesoporous TiO_2/WO_3 nano honeycomb photoelectrode was attributed to its lower band-gap, greater surface area, and higher charge separation capability [168].

Sharma *et al*. synthesized a nanostructured thin film of Zn-Fe_2O_3 with an underlying Fe-TiO_2 thin film and employed it in PEC water splitting. The underlying Fe-TiO_2 films of various thicknesses (0.32, 0.65, and 0.97µm) were grown on ITO through a sol-gel spin coating procedure to explore the significance of its thickness on the PEC performance of Zn-Fe_2O_3. PEC results show photoelectrode with an overall thickness of 0.89 µm (0.65 µm thick Fe-TiO_2 and 0.24 µm thick Zn-Fe_2O_3) shows an uppermost J_{sc} of $748\ \mu A/cm^2$ at 0.9 V_{SCE} and solar to the hydrogen conversion efficiency of 0.47 % under a 1.5AM filter solar simulator. This boost in the PEC activity was credited to the effective parting of photoexcited charged carriers at the interface, decrease in resistance and enhancement in the light absorption capability [169].

1.4.5 Gas-phase Precursor Method

In the gas-phase precursor method, the precursor used is in a gaseous phase. The coating was performed by activating the precursor gas atom through thermal energy or a plasma

The Art of writing only for samples use

source. Below are descriptions of the various methods employed in the gas phase precursor process.

1.4.5.1 Chemical Vapor Depositions (CVD)

CVD is a multipurpose and suitable process for depositing single or multi-component thin films with controlled stoichiometry and morphology over a wide range of substrates [170]. CVD has been discovered to be a very useful technique in fabricating materials that can be used in a wide variety of fields like functional semiconductors, PEC cell, photocatalysis, DSSC, optoelectronics, optical, wear & corrosion resistance coating, monolithic parts and still this field is expanding continually with a good pace [171-174].

CVD is characterized as the deposition of a stable solid product on a heated substrate using a chemical reaction and/or gaseous reactant dissociation in an activated atmosphere (plasma, heat, or light). Deposition comprises a homogeneous gas-phase reaction in the gas phase or a heterogeneous chemical reaction on or nearby a heated substrate that results in the development of thin films or powders. The CVD process can use a variety of chemical reactions to deposit thin films, including hydrolysis, pyrolysis, reduction, carburization, oxidation, disproportionation, and nitridation. CVD reactions are influenced by numerous parameters like the chemistry of reaction, thermodynamics, mass transport, pressure, the kinetics of the reaction, temperature, and chemical activity of species existing in the reaction compartment [107].

Some distinctive advantages of CVD are: (i) very useful to deposit dense and pure materials (ii) a uniform film with good reproducibility rate and adhesion can be produced (iii) controlling the CVD parameters allows us to easily monitor the surface morphology, crystal structure, and alignment of the CVD product. Furthermore, one can easily change the deposition rate in CVD, a low deposition pace is best for growing epitaxial thin films, which have a lot of applications in microelectronics. However, for dense protective coating deposition, high-rate deposition is favored, with rates exceeding tens of µm per hour. In CVD, a large range of chemical precursors, such as organometallics, hydrides, and halides, can be used thus a wide range of materials can be deposited including

The Art of writing only for samples use

metals, sulfides, carbides, nitrides, and oxides [175]. A schematic diagram of CVD and film growth mechanism is shown in **Figure 1.25.**

However, there are also some disadvantages associated with CVD like (i) some of the precursors used are toxic, flammable, explosive, and carcinogenic. However, this drawback can be overcome by using certain other versions of CVD such as Combustion CVD and Electrostatic Spray Assisted Vapour Deposition (ESAVD) that uses more environment-friendly precursors (ii) since dissimilar precursors have different vaporization rates, it is very challenging to deposit multi-component materials with proper stoichiometry using multi-source precursors; however, this shortcoming was controlled by using single-source precursors. (iii) Some CVD variants, such as plasma-assisted CVD, low pressure or ultra-Vacuum CVD, and photo-assisted CVD, use complex and costly reactor and/or vacuum systems, increasing fabrication cost. However, several CVD variants do not require expensive reactor and vacuum systems, such as Aerosol Assisted CVD and Flame Assisted CVD. As a result, these low-cost versions can be used instead of the high-cost variants. [175].

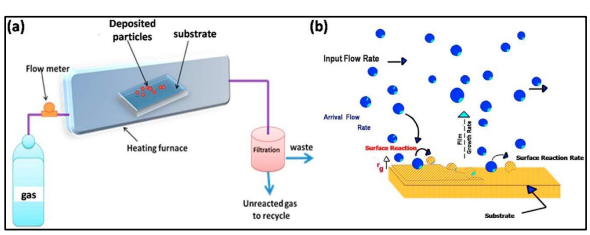

Figure 1.25: (a) Schematic diagram of CVD **(b)** film growth mechanism by a CVD method. [107]

Gardecka *et al.* synthesized highly nanostructured TiO_2 thin film on FTO substrate with the help of pulsed-pressured metal-organic CVD by varying deposition parameters to tune the synthesized TiO_2 photoelectrode properties such as the thickness

The Art of writing only for samples use

of the deposited film, a fraction of rutile and anatase phases, and surface topography. It was reported that photoelectrode which contains both anatase and rutile phase shows synergetic enhancement in PEC performance as compared to anatase phase alone with IPCE above 80% in the UV region and J_{sc} of $\sim 1.2\ mA/cm^2$ at 1.23V_{RHE}. The co-deposited carbon was discovered to be critical in templating the formation of dendritic TiO2 morphology, but since carbon repressed water splitting it was extracted by the annealing process leaving behind greatly active nanostructured photoelectrode [176].

Jeong *et al*. produced a unique vertically ordered ZnO-TiO_2 core-shell nanowire (NWs) on a silicon wafer utilizing CVD and employed it as a photoelectrode in PEC water splitting. PEC measurement shows that amorphous-crystalline ZnO-TiO_2 core-shell nanowire displays an optimum J_{sc} of $1.23 mA/cm^2$ that is 2.4 times that of pure ZnO NWs. This improvement in the PEC activity is accredited to the synergetic effect of the amorphous-crystalline core-shell heterostructure that results in proficient separation of photoexcited charge carriers and rapid transport of charges through the 1D ZnO nanowires [177].

Arzaee *et al*. successfully converted thin film of α-Fe_2O_3 nanoflakes into 3-D nanoflower using AACVD by simply supplying an excessive amount of oxygen and controlling the deposition rate. It was acquired that excessive oxygen supply enables the growing process to be directed by (110) crystal plane, while high deposition period results in the conversion of α-Fe_2O_3 nanoflakes into α-Fe_2O_3 nanoflowers. PEC measurement shows that film deposited for 40 min show an uppermost J_{sc} of $585 \mu A/cm^2$ at 1.2$V_{Ag/AgCl}$. It was credited to the enlarged surface area and better light absorption capability of nanoflowers. However, films obtained after 10- or 20-min deposition show less J_{sc} due to the small surface area and poor light absorption capability of nanoflakes as compared to nanoflowers. Further, an increase in deposition time up to 60 min results in a decrease in the J_{sc} due to the short diffusion length of α-Fe_2O_3 [178].

Khan *et al*. fabricated cobalt-doped ZnO thin films by using AACVD. To study the influence of Co doping on PEC efficiency, different cobalt concentrations (2, 5, 10,

and 15%) were doped. PEC measurements show that among all the photoanode ZnO thin film doped with 15 % Co shows the highest J_{sc} of about $0.97 mA/cm^2$ at $0.7V_{RHE}$ and double-layer capacitance of $0.65\ mF/cm^2$. The increment in PEC activity of Co-doped ZnO thin film as compared to bare ZnO was credited to the improvement in absorption range and efficient charge separation and transport due to Co doping [179].

1.4.5.2 Atomic Layer Deposition (ALD)

ALD is a vapor phase deposition method that can develop a wide range of thin-film materials. ALD has a great capability for developing insulators, semiconductors, and energy conversion technologies. ALD is like that of CVD, with the exception that in ALD, the precursor gases are added in a row. Unlike CVD, where several precursor gases can be pumped at the same time, the ALD chamber only contains one precursor gas at a time [107]. ALD uses alternate pulses of gas-phase precursors on the substrate surface that results in subsequent chemisorption or surface reaction of the substrate. This individual gas-phase reaction with the substrate surface is termed a "half-reaction" and produces only one portion of the synthesis layer on the substrate. Throughout each half-reaction, the required precursor is pulsed into a compartment under vacuum and is allowed to completely react with the substrate surface for a set amount of time. After each half-reaction, the reaction compartment is washed with inert carrier gases to eliminate any unreacted precursor gas or reaction by-product. It is then trailed by the counter reactant pulse and purging, producing a single layer of the required material. This method is repeated multiple times till the appropriate thickness of the required material is obtained (**Figure 1.26)** [180].

Some of the distinguished advantages of ALD are summarized as; (i) formation of uniform and conformal growth of complex nanostructure as compared to CVD and PVD, (ii) definite control over the film thickness, using the layer-wise deposition-the thickness of the film can be simply adjusted by the number of ALD cycle, (iii) compositional control by tailoring ALD cycles [180]. The main drawback related to ALD is the slow deposition rate due to the long cycle time consumed in pulsing and purging precursors and the layer-wise type of deposition. Most of the ALD cycle rates are found to be in the

The Art of writing only for samples use

order of 100-300 nm/h. The deposition rate is found to be reliant on the reactor engineering and aspect ratio of the substrate. The time for pulsing and purging precursors increases as the reactor's volume and the surface area grow. High aspect ratio substrate also requires high time for pulsing and purging precursors to enable the precursor gas to diffuse into trenches and other 3-D features [180].

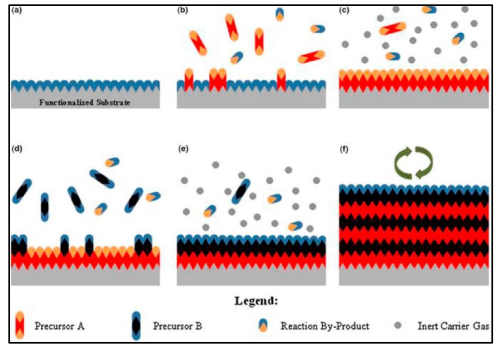

Figure 1.26: Schematic diagram of ALD process **(a)** functionalization of the substrate **(b)** The substrate interacts with Precursor A, which is pulsed. **(c)** Using an inert carrier gas to purge. **(d)** The substrate reacts with Precursor B, which is pulsed**. (e)** purging again using an inert carrier gas. **(f)** Steps (b-e) are repeated again and again till the required thickness is attained. [180]

Zhang *et al.* successfully deposited CdTe QDs on TiO_2 nanorod array film (NRA) deposited on FTO using electrochemical atomic layer deposition (ECLD). Through the ECLD technique, the size of CdTe QDs was found to be easily monitored by the deposition cycle, and hence the uniform distribution of CdTe QDs can be achieved. An optimum short circuit current density of $15.43\ mA/cm^2$ and photoconversion efficiency of 7.9% was attained for TiO_2 NRA photoelectrode deposit with CdTe after 120 cycles. [181]

The Art of writing only for samples use

Steier *et al.* use a low-temperature ALD approach to deposit smooth, conformal, pure phase and crystalline α-Fe_2O_3 on FTO substrate that do not require post-annealing treatment. It was found that the ALD using *N, N*-(dimethylaminomethyl-) ferrocene, and ozone as precursors gave α-Fe_2O_3 with extremely low contamination of carbon (0.2 atom %). By growing a TiO_2 underlayer as a dopant source and as a hole blocking layer, the α-Fe_2O_3 film having a thickness of 10nm was recognized as the optimum path length for effective charge collection with an optimum J_{sc} of $0.8\ mA/cm^2$**.** It is the uppermost J_{sc} ever recorded for pristine α-Fe_2O_3 thin film. It was also reported that for α-Fe_2O_3 films thicker than 10 nm, the PEC activity was confined due to the space charge width, however, for α-Fe_2O_3 films thinner than 10 nm light absorption capability was found to be the limiting factor.[182]

Wang *et al.* synthesized heterojunction of ZnO decorated on hydrogen treated TiO_2 nanotube array (H-TiO_2) using the ALD technique. The thickness of ZnO was accurately governed by the number of ALD cycles. A higher growth rate of ~2.7 Å/cycle is observed for H-TiO_2 as compared to air-treated TiO_2 (A-TiO_2), ~2.3 Å/cycle. After coating the TiO_2 nanotube with 42 nm of ZnO ALD an optimum J_{sc} of 0.67 mA/cm^2 for H-TiO_2 was obtained while A-TiO_2 showed $0.36\ mA/cm^2$at $1.23V_{RHE}$. The highest PEC activity of H-TiO_2 was credited to high electronic band bending, improve photoresponse in the UV and visible portion owing to the oxygen vacancy [183].

1.5 Photoelectrode Efficiency

The operating conditions of a photoelectrode have a significant impact on the obtainable photocurrent and its whole performance. Experiments should typically be conducted under a set of specific protocols, which include irradiation with an intensity of about 100 mW/cm^2 corresponding to 1 sun at AM 1.5 G and spectral distribution. Since various semiconductors are stable in various electrolytes, prescribing a single universal electrolyte is a much more complex task. The electrolyte used, the concentration of the electrolyte, and the pH of the solution should always be defined. Generally, there are four different ways to measure efficiency for a photoelectrochemical cell.

The Art of writing only for samples use

1.5.1 Solar-to-hydrogen Efficiency (STH)

STH is calculated by dividing the chemical energy of H_2 produced divided by the solar energy input. As shown in equation (1.5), the chemical energy of the H_2 produced can be determined by multiplying the rate of H_2 production (mmol H_2/S) by the change in Gibbs free energy per mole of H_2 (G=237KJ/mol at 25°C) [184, 185].

$$\mathrm{STH} = \left[\frac{(\mathrm{mmolH_2/S}) \times 237\mathrm{KJ/mol}}{\mathrm{p_{total}}\ (\mathrm{mw/cm^2}) \times \mathrm{A/(cm^2)}}\right]_{\mathrm{AM1.5G}} \ldots\ldots\ldots\ldots\ldots\ldots\ldots\ldots\ldots\ldots\ldots\ldots (1.5)$$

Here p_{total} is the incident illumination power density (mW/cm^2), where A is the illuminated area of the electrode (cm^2). Equation 5 can be useful if the exact amount of hydrogen production is calculated using gas chromatography or mass spectroscopy. Otherwise, STH can also be calculated using equation 6 in which 1.23V is the theoretical voltage for splitting water, J_{ph} is the photocurrent density measured, n_f is the faradic efficiency for H_2 evolution. The equation (1.6) is only valid, if the measured photocurrent corresponds directly to the molar H_2 generation rate [184, 185].

$$\mathrm{STH} = \left[\frac{\left(\mathrm{J_{ph}(mA/cm^2)}\right) \times (1.23\mathrm{V}) \times \mathrm{n_f}}{\mathrm{p_{total}}\ (\mathrm{mW/cm^2})}\right]_{\mathrm{AM1.5G}} \ldots\ldots\ldots\ldots\ldots\ldots\ldots\ldots (1.6)$$

1.5.2 Applied Bias Photon-to-Current Efficiency (ABPE)

STH is utilized to find the overall water splitting performance of a PEC cell when no external biased is applied. However, if an external bias is applied between the working electrode and the counter electrode, a new efficiency value instead of STH is used which is ABPE. The following equation (1.7) can be used to describe ABPE [185].

$$\mathrm{ABPE} = \left[\frac{\left|\left(\mathrm{J_{ph}(mA/cm^2)}\right)\right| \times (1.23 - |\mathrm{V_b}|) \times \mathrm{n_f}}{\mathrm{p_{total}}\ (\mathrm{mW/cm^2})}\right]_{\mathrm{AM1.5G}} \ldots\ldots\ldots\ldots\ldots\ldots (1.7)$$

ABPE cannot be used to represent true STH, it just serves as a diagnostic tool for material development. Secondly, ABPE cannot be used in the electrolyte containing sacrificial agents (donors or acceptors) [184]**.**

1.5.3 Incident Photon-to-Current Efficiency (IPCE)

IPCE is used to determine the efficiency of electron/hole converted from photons at an individual wavelength of light on a single photoelectrode level. IPCE measurements are carried out by using the chronoamperometric measurement technique (Potentiostat). A bias is applied between the working electrode and the counter electrode (for a two-electrode experiment) or reference electrode (for a three-electrode experiment), while the photocurrent density is measured with exposure of the working electrode to monochromatic light at a specific wavelength [184]. Thus, IPCE as a function of wavelength (λ) is provided by equation (1.8) [185].

$$\mathrm{IPCE} = \left[\frac{(1240) \times J_{ph}(mA/cm^2)}{\lambda \times p_{total}\ (mW/cm^2)}\right]_{AM1.5G} \quad \ldots\ldots\ldots\ldots\ldots\ldots\ldots\ldots\ldots\ldots \quad (1.8)$$

1.5.4 Absorbed Photon-to-Current Efficiency (APCE)

STH and IPCE measurements also include those photons which are reflected. Thus, to determine the true output of material, these losses must be subtracted, and efficiency must be calculated using only those photons that are absorbed. APCE is particularly useful for thin films as it allows to find out the optimal balance between the maximum path length for photon absorption against the minimum effective e^-/h^+ transfer distance inside a material. The following equation (1.9) can be used to find out APCE [184, 185].

$$\mathrm{APCE} = \left[\frac{J_{ph}(mA/cm^2) \times 1240(V \times nm)}{P_{mono}(\frac{mw}{cm^2}) \times \lambda(nm) \times (1 - 10^{A})}\right]_{AM1.5G} \quad \ldots\ldots\ldots\ldots\ldots\ldots\ldots (1.9)$$

1.6 Semiconductor Material and Properties

Semiconductor materials have a conductivity that lies somewhere between metal and insulators. Solids are classified as semiconductors if they have conductivity in the range of 10^{-10} to 10^{4} $Ohm^{-1}cm^{-1}$ [186]. The VB and CB of semiconducting material neither overlap nor very far, but are narrow enough to allow electrons to excite from VB into the CB at

The Art of writing only for samples use

temperature T > 0 K. Upon excitation of electrons into CB, free electrons in the CB act as a negative charge carrier while the holes left behind in the VB act as a positive charge carrier [187, 188]. Depending on compositions semiconductors are divided into two types.

1.6.1 Intrinsic Semiconductor

Intrinsic semiconductors are pure or undoped semiconductors in which the number of electrons in the CB matches the number of holes in the VB. Since electrons cannot pass to the CB, the intrinsic semiconductor has similar properties to an insulator. When the temperature is increased or heat energy is applied, some valence electrons are lifted into the CB, leaving holes behind. The electrical conductivity of intrinsic semiconductors is typically low, and it increases as temperature rises. Silicon and Germanium in their crystalline form, without any dopant, are intrinsic semiconductors [189].

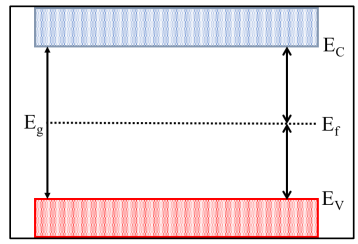

Figure 1.27: Energy band diagram of an intrinsic semiconductor.

1.6.2 Extrinsic Semiconductor

A semiconductor's electrical conductivity can be improved by doping with appropriate dopant atoms to form an extrinsic semiconductor (e.g. phosphorus-doped into silicon) [189]. During the preparation of extrinsic semiconductors, the amount and form of impurity applied to the material must be carefully monitored [186]. As opposed to intrinsic semiconductors, extrinsic semiconductors have a higher electrical conductivity.

The Art of writing only for samples use

Depending on the dominant energy carrier extrinsic semiconductors are categorized into two different categories [189].

1.6.2.1 n-type semiconductor

n-type semiconductors are extrinsic semiconductors that have a higher number of electrons in their CB than holes in the VB. Simply in *n*-type semiconducting materials, the mainstream carriers are electrons, while holes are marginal carriers.[187, 188]. In *n*-type semiconductors, dopant atoms serve as electron donors, and their energy levels are close to the semiconductor's CB, but far from VB. It's important to remember that *n*-type semiconductors are electrically neutral since the equivalent nuclear charge of the dopant atoms balances the net negative charge of electrons.

1.6.2.2 p-type semiconductor

To make *p*-type semiconductors, dopant atoms with one less electron to complete bonding in the host crystal are added to produce an acceptor level near the VB. As a result, electrons can be quickly excited from the semiconductor's VB into the localized energy levels of dopant atoms (acceptor), leaving holes in the semiconductor's VB. Thus in *p*-type semiconductors, the hole density in the VB is much higher than the electrons density in the CB, so holes are the mainstream carriers and electrons are the marginal carriers [187, 188]. The net positive charge in the VB of the semiconductor is neutralized by electrons in the intrinsic energy levels of dopant atoms, so the *p*-type semiconductors are electrically neutral.

1.6.3 Fermi Level (E_f)

E_f is an electronic energy level of semiconductors in which the probability of finding an electron is 1/2, and therefore all semiconductor electronic energy levels below the fermi energy level are occupied, whereas those above the fermi energy level are likely to be empty [98, 187]. The E_f in intrinsic semiconductors is located approximately at the midpoint of the bandgap i.e., between the VB and the CB **(Figure 1.27)**. As donors or acceptor impurities are doped in intrinsic semiconductors, the E_f will shift accordingly toward the

The Art of writing only for samples use

semiconductor's CB or VB. The E_f is just below the CB in an *n*-type semiconductor **(Figure 1.28 a)**, but just above the VB in a p-type semiconductor **(Figure 1.28 b)** [187].

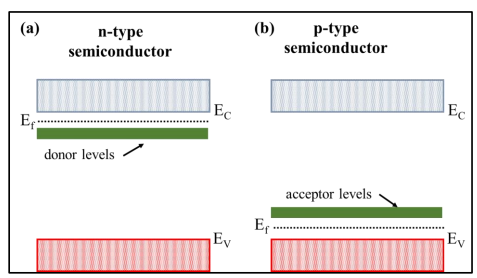

Figure 1.28: Energy band diagram **(a)** n-type and **(b)** p-type semiconductors.

1.6.4 Properties of the Semiconductors-electrolyte interface and Band Bending

When a semiconductor with a bandgap of E_g is dipped in an electrolyte solution, a junction is created between the semiconductor and the electrolyte. The electrochemical potential of the electron inside a semiconductor is determined by their E_f, while in a liquid electrolyte, the electrons' electrochemical potential can be determined by their redox potential which is given by the Nernst equation [187, 190].

$$E_{redox} = E^0_{redox} + \left(\frac{RT}{nF}\right) \times \ln\left(\frac{C_{oxi}}{C_{red}}\right) \ldots\ldots\ldots\ldots\ldots\ldots\ldots\ldots\ldots\ldots\ldots\ldots\ldots\ldots\ldots\ldots \quad (1.10)$$

Where $E°_{redox}$ is the standard redox potential, F is the Faraday constant, n is the number of electrons utilized in the redox reaction, R is the general gas constant, and C_{ox} and C_{red} are the oxidized and reduced species concentrations, respectively. Due to a difference in electrochemical potential between the E_f of the semiconductor and the redox potential of the electrolyte, shifting of electric charge occurs between semiconductor and electrolyte until the E_f of the semiconductor becomes equivalent to the redox potential of

the electrolyte, and thus equilibrium is established [80, 191]. When an *n*-type semiconductor is submerged in an electrolyte, electrons are transported from the semiconductor surface to the electrolyte since the E_f of an *n*-type semiconductor are generally higher than the redox potential of the electrolyte [187]. The passage of electrons from the semiconductor to the electrolyte causes the formation of a space-charge layer on both sides of the junction, which extends into the electrode for a distance of 10 to 1000 nm and has a different charge distribution than the bulk material on both sides of the junction [187]. Since electrons are the major charge carriers in *n*-type semiconductors, depletion of electrons in the space-charge area occurs under equilibrium conditions, and this region is termed the depletion layer, which is defined by an excess positive charge (**Figure 1.29 b**). An electric field is developed between the semiconductor and electrolyte due to the transfer of electrons. The electric field between the semiconductor and electrolyte causes shifting of the energy band edges, known as band bending [98, 187, 188]. The direction in which the energy band of the semiconductor bends can be predicted by considering the electrostatic force experienced by the electron while moving through the semiconductor electrolyte interface. In *n*-type semiconductors, band bending occurs in an upward direction because of the repulsive force among electrons in the semiconductor and negatively charged ion (reduced species) of electrolyte [187, 192].

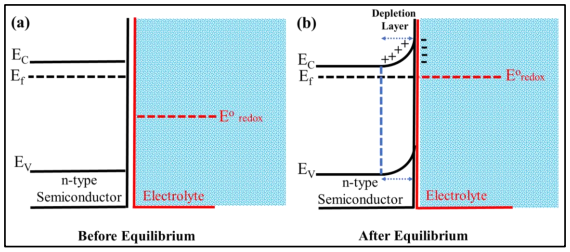

Figure 1.29: Energy band diagram of **(a)** n-type before equilibrium and **(b)** after equilibrium.

However, when a *p*-type semiconductor is dipped inside an electrolyte electron movement will occur in the opposite direction as compared to an *n*-type semiconductor since **t**he E_f of the *p*-type semiconductor is typically lower than the electrolyte redox potential, directing electrons from the electrolyte into the semiconductor. This movement of electrons alters the distribution of charges on either side of the semiconductor-electrolyte interface resulting in the development of the space charge region. Electrons that cross the semiconductor-electrolyte interface gather near the semiconductor surface, such a region is named as accumulation region **(Figure 1.30b)**. Due to the attractive force between electrons in the semiconductor and positively charged species (oxidized species) of electrolyte, the energy of electrons decreases as they come close to the semiconductor surface. Therefore, the energy band of the *p*-type semiconductor bends downward when dipped in an electrolyte [187]**.**

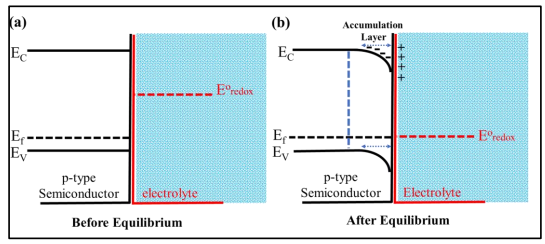

Figure 1.30: Energy band diagram of **(a)** p-type before equilibrium and **(b)** after equilibrium.

1.6.5 Flat Band Phenomenon

If the Fermi level of the electrode becomes equal to the electrochemical potential of the electrolyte both under dark and illumination, no transfer of charge (electric field) occurs as a result there is no band bending (Figure 1.3**1**), termed flat band potential (E_{fb}) [187]. E_{fb} is found to be dependent on ion absorption, orientation (crystallographic) of the exposed surface, surface defects, and surface oxidation processes [193].

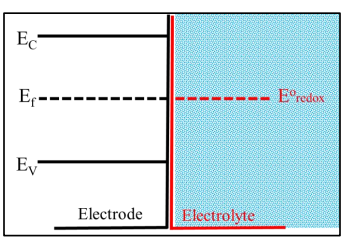

Figure 1.31: Fermi level of the electrode becomes equal to the electrochemical potential of the solution in the flat band potential phenomenon.

1.7 TiO_2 as a Promising Material for PEC Water Splitting

One of the principal challenges for effective PEC water splitting is to find out perfect semiconductor materials that can be used as efficient photoelectrodes. Among several types of semiconductors applied for PEC studies, TiO_2 due to its desirable properties like low cost, non-toxicity, chemical stability, resistance toward photo corrosion, and suitable CB and VB position for desired PEC water splitting is a favorable material for photoelectrodes [194-197].

1.7.1 Crystal Structure of TiO_2

TiO_2 occurs in three different polymorphic forms in nature: each of which has an electronic bandgap in the nearby UV region. The bandgap energy of TiO_2 varies depending on its polymorph, with tetragonal rutile, tetragonal anatase, and brookite having bandgap energies of 3.0, 3.2, and 3.3 eV, respectively [198-201]**.** These TiO_2 polymorphs all feature TiO_6 octahedra however, they differ primarily in octahedron unit distortion and sharing of corners and edges. Crystalline anatase TiO_2 possesses distorted octahedral (O_h) geometry in which a single Ti atom is enclosed by six oxygen atoms in an elongated octahedral configuration (D_{2d}) showing axial symmetry. However, in rutile (D_{2h}) both equatorial and axial bond angle and bong length distortion occur [202, 203]. The rutile phase is by far the most stable phase under a wide range of temperatures and

pressures up to 60 kbar [204, 205]. Stronger distortions in brookite result in the loss of local symmetry and the creation of C1-symmetric TiO_6 units [202, 203]. Brookite is the most complex of the three types, with a greater cell volume, least dense, and seldomly used in experiments [206]. Anatase phase share corner, the rutile phase share edges, while the brookite phase share corner and edges (**Figure 1.32**). Cotunnite is also another phase of TiO_2 that exists under high temperature and pressure and is additionally one of the hardest materials reported [207].

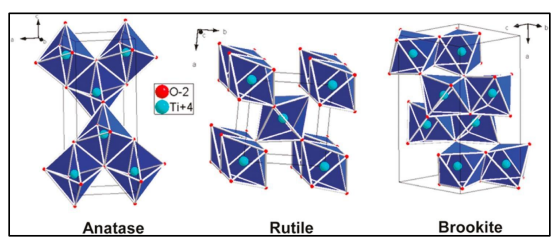

Figure 1.32: Crystal structures of TiO_2 polymorphs. [203, 208]

1.7.2 Nanostructured TiO_2 Photoelectrodes

Different kinds of TiO_2 nanostructures have been inspected for PEC studies, which can be categorized into particulate, 1-dimensional (1-D), 2-dimensional (2-D), and 3-dimensional (3-D) nanostructures based on their geometry configurations. The nanoparticulate TiO_2 structure, compromised of an interrelated system of nanometer-sized crystals, has been commonly used as a substrate for PEC studies offering a huge surface area and strong absorption capacity for the photosensitizer [209]. 1-D and 2-D TiO_2 nanostructures were aimed to allow the direct and quick flow of photoexcited electrons and holes and to reduce the charge recombination [210, 211]. While 3-D TiO_2 nanostructures like branched TiO_2, nano-forest TiO_2, nano-flowered TiO_2, etc. have been planned to upsurge the surface area, boost the light-harvesting capability, and superior charge transfer capability [212-214]. Recently, a new concept of tailoring the crystal-faced of TiO_2

nanostructure has gotten significant attention as enhanced PEC performance has been attained by adjusting the ratio of the exposed facet in the crystal lattice [215, 216].

1.7.2.1 Nanoparticulate TiO_2 Nanostructures

Since the exchange of solar energy into chemical energy in PEC cells happens at the photoelectrodes' surface, investigation of a metal oxide-based semiconductor with a large surface area is highly preferred. Among the numerous capable materials that can be used, nanoparticulate TiO_2 with an enlarged surface area has gotten significant attention in recent years. [217-219]. Nanoparticulate TiO_2 has been thoroughly explored in DSSC. Significant contributions on TiO_2 based DSSC have been made by Michael Grätzel and coworkers by systematically studying the effect of film thickness, particle size, morphology, etc. on solar energy conversion efficiencies [220, 221]. For dye-sensitized TiO_2 photoelectrodes, optimum solar conversion efficiencies of around 12.3% have been reached, which are comparable to traditional Si-based PV cells [222]. The significant boost in the photoconversion efficiency is credited to the rapid charge transfer from dyes molecules to TiO_2 nanoparticles, large specific surface area, huge quantities of loaded dye, and effective partitioning of photoexcited charge carriers/electron and holes. Motivated by the excellent performance shown by TiO_2 nanoparticles in DSSC, nanoparticulate TiO_2 was then introduced to study PEC water splitting [208].

Zhao *et al*. produced TiO_2 nanoparticles photoelectrode with a well-defined crystalline anatase phase and a particle size less than 20 nm using the potentiostatic anodization technique. However, the synthesized photoelectrode with pure anatase phase shows inadequate J_{sc} of $\sim 40\ \mu A/cm^2$ [223]. Jing *et al.* synthesized mixed-phase (anatase and rutile) TiO_2 nanoparticles photoelectrode on FTO using dip-coating followed by calcination (700°C for 16 h). Due to the effective charge partitioning induced by the combined phases, the lifespan of the photoexcited electron and hole was extended and shows outstanding PEC behavior against organic pollutants degradation. Notable J_{sc} of $1\ mA/cm^2$ was attained at 0.2 $V_{Ag/AgCl}$ for glucose degradation [224].

Vinogradov *et al.* produced Fe-doped TiO_2 photoelectrode using a low-temperature sol-gel process. It was discovered that Fe-doping enhances the light absorption efficiency of TiO_2. PEC studies show that 7 % Fe-doped TiO_2 photoelectrode shows a maximum J_{sc} of $54\ \mu A/cm^2$ that is 3.6 times greater than pristine TiO_2 photoelectrode ($15\ \mu A/cm^2$) under visible light irradiation [225]. Bui *et al.* fabricate Si-doped TiO_2 nanoparticle photoelectrode with anatase crystalline phase by a hydrothermal approach employing acetic acid as a solvent. The PEC measurements show a maximum J_{sc} of 54.4 μA for 15 mol % Si-doped TiO_2 while pristine TiO_2 photoelectrode shows a J_{sc} of 16 μA. Si doping assists the movement of photogenerated electrons towards the cathode, thus minimizing the recombination pace of photoexcited electron and hole pairs [218].

1.7.2.2 1-D TiO_2 Nanostructures

One of the main disadvantages of using TiO_2 nanoparticulate thin film photoelectrodes for PEC application is their low electron diffusion coefficient as compared to single-crystal TiO_2 which results in a decrease in PEC efficiency. This decrease in PEC efficiency may be **d**ue to extreme electron trapping at TiO_2 nanoparticle grain boundaries. To overcome this drawback 1-D TiO_2 nanorods (NRs), nanowires (NWs), and nanotubes (NTs) were designed that provide direct electron transfer pathways and high electron mobility resulting in a higher charge transfer pace [226, 227]. As a result, 1-D TiO_2 nanostructures, mainly nanotube, and nanowires arrays have acquired a lot of attention and have been extensively used as photoelectrodes.

Wolcott *et al.* synthesized 1-D TiO_2 nanorod array (NRAs) using oblique angle deposition on ITO substrate and employed them as photoelectrode for PEC application. The synthesized nanorod has a length of approximately 800-1100 nm and a width of 45-400 nm. A high rate of electron collection at ITO was observed as revealed by the IPCE measurement (79% at 350 nm). This was accredited to the rapid upright charge transfer through nanorods, less surface defect, and reduced charge recombination. Although total STH efficiency (0.1% at an applied potential of $1.0V_{Ag/AgCl}$) was comparatively low, it

gives an insight into how to boost the PEC performance by varying the nanowire size and improving the visible light absorption capability through doping and sensitization [228].

Hwang *et al.* produced a rutile phase TiO_2 nanowire on an FTO substrate using a hydrothermal technique and reported the impact of nanowire length and surface structure on PEC performance. **Figures 1.33(a) and (b)** show images of samples prepared at various times. PEC results show that the J_{sc} shows a nonlinear dependency on the length of nanowires and an optimum J_{sc} of $0.73\ mA/cm^2$ ($1.5V_{RHE}$) was obtained for $1.8\ \mu m$ lengths as illustrated in **Figures 1.33 (c) and (d)**. Epitaxial rutile TiO_2 shell was also coated over TiO_2 nanowire using ALD to increase charge collection proficiency as a result 1.5 times enhancement in the photocurrent was observed [229].

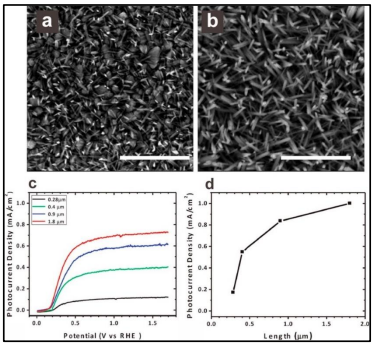

Figure 1.33: SEM images of TiO_2 NWs produced hydrothermally **(a)** 50min **(b)** 60 min. **(c)** LSV studies of the as-prepared NWs having different lengths **(d)** Comparison of J_{sc} at 1.5V vs RHE for different NWs length [229].

Sun *et al.* produced perpendicularly arranged single-crystalline rutile phase TiO_2 NRAs on FTO by hydrothermal route. The impact of temperature, time, and precursor on

PEC properties, crystal structure, and morphology of the TiO_2 NRA films was investigated in detail. The crystallinity and length of the nanorod were found to increase considerably with temperature but only marginally with time. With increasing reaction temperature, both J_{sc} and external quantum efficiency (EQE) of TiO_2 NRAs initially enhanced and then lessened, however, less improvement was observed with changes in the growth period. Among all the synthesized photoanode TiO_2 NRs having lengths of 2-3 μm produced at 160-170 °C for 1h shows the best PEC performance [230].

Xie *et al.* developed N-doped TiO_2 NRAs by calcining TiN NRAs synthesized using the oblique angle deposition method. The synthesized TiN NRA was calcined at 330 °C for various periods (120, 60, 30 15, 5 minutes). The bandgap of the synthesized N-doped TiO_2 NRAs shows great variation with changing annealing time. According to PEC studies, all the N-doped TiO_2 NRAs show enhanced J_{sc} under visible light irradiation, particular the one annealed for 15 min shows the uppermost J_{sc} due to optimum N dopant quantity. This confirms that *in-situ* doping during synthesis is one of the easy and potent approaches [231].

Tang *et al.* produced Sulphur (S) doped TiO_2 nanotubular arrays (NTAs) by potentiostatic anodizing titanium foil succeeded by calcining at 380 °C in an H_2S flow. The as-synthesized S-doped TiO_2 NTAs show a 10-times increment in the J_{sc} in comparison to the bare TiO_2 NTAs. The rise in PEC performance was assigned to the substitution of the oxygen atom by S ion which resulted in the shifting of the absorption edge from 400 to 650 nm narrowing the bandgap [232].

1.7.2.3 2–D TiO_2 Nanostructures

Just like 1-D nanostructures, 2-D TiO_2 nanostructures also provide direct electron transfer pathways and hence have attractive electrical and optical properties. However, what defines 2-D nanostructures more superior is their large specific surface area and additional active sites. Various 2-D nanostructures like TiO_2 nanobelts/nanoribbon/ nanopowder have been broadly investigated for photocatalytic applications, however, they also have some success stories in PEC applications [233, 234].

Liu *et al.* synthesized TiO_2 nanosheets photoelectrodes and studied their PEC application by individually depositing various transition metal oxide clusters (CoO_x, FeO_x, NiO_x, MnO_x, and CuO_x). It was found that the nanosheets morphologies assist the charge carrier partitioning and offer an adequate site for the deposition of metal oxide clusters that work as hole trap sites in PEC reactions. PEC measurements show that among all the metal oxide cluster deposited TiO_2 nanosheets, an uppermost J_{sc} of $55\ \mu A/cm^2$ at $0.5V_{Ag/AgCl}$ was observed for CoO_x deposited TiO_2 nanosheets while pristine TiO_2 nanosheets display a J_{sc} of $8\ \mu A/cm^2$ under equivalent experimental conditions [233].

Zhou *et al* used solvothermal treatment of TiN in an acidic solution of $NaBH_4$ to create N-doped TiO_2 (anatase) nanosheets with (001) dominant facet (**Figure 1.34 a and b)** to investigate their photocatalytic degradation of organic pollutant activity and PEC water splitting capabilities. The synthesized N-doped TiO_2 nanosheets show high PEC efficiency, under visible light and a maximum J_{sc} of $400\ \mu A/cm^2$ was acquired w is 3.3 times greater than J_{sc} shown by N-doped P25 $(123\ \mu A/cm^2)$ [235]. Wang et al were successful in growing nanosheets shaped TiO_2 on Ti foil *via* a facile hydrothermal route. The synthesized nanosheets show an optimum J_{sc} of $0.15\ mA/cm^2$ at $0V_{Ag/AgCl}$, which is credited to the highly reactive nature of the (001) facet exposed nanosheets [236].

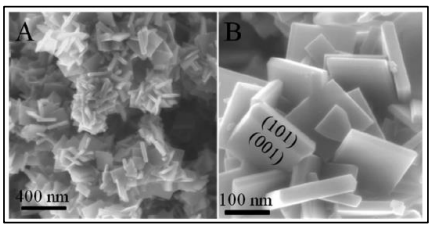

Figure 1.34: (a) low and **(b)** high magnification SEM images of N-doped TiO_2 nanosheets [235].

1.7.2.4 3-D TiO_2 Nanostructures

In addition to the advancement in 1-D/2-D TiO_2 nanostructures, further research was undertaken to better architect TiO_2 geometrical configurations to obtain enlarged surface area without disturbing their direct charge transfer capability. With this concern, immense efforts are being devoted to developing 3-D TiO_2 structures with optimized branched designs [237-241].

Cho *et al.* synthesized single-crystalline branched TiO_2 NRs photoelectrode using hydrothermal and CBD techniques as shown in **Figure 1.35 (a-d)**. Branches, as well as the main trunk of the branched TiO_2 NRAs, are singly crystallized rutile phases. The ultra-thin branches were found to be useful for the effective transport of holes to the semiconductor/electrolyte interface for water oxidation reaction as most of the charge carriers are produced within the diffusion length of the semiconductor/electrolyte interface, thus minimalizing the recombination rate. Secondly, the branched TiO_2 architecture also provides a large contact area (4-fold enhancement in the surface area) with the electrolyte, enhances the light-capturing capability, and provides a very conductive route for the direct transfer of photogenerated electrons. PEC studies show that branched TiO_2 NRs show optimum J_{sc} of $0.83\ mA/cm^2$ at $0.8V_{RHE}$, which is around 2 times greater than the J_{sc} shown by TiO_2 NRs devoid of branches (**Figure 1.35e)** [241]**.** These branched TiO_2 NRs nanostructure design was then utilized in CdS QDs sensitized PEC application by Su *et al.* Due to innovative branched structure and efficient charge separation capability a significantly improved J_{sc} of $\sim 4\ mA/cm^2$ at $0V_{Ag/AgCl}$ was noted [240].

Yang *et al.* explored the PEC capability of 3D-branched TiO_2 photoelectrode having core-shell architecture - the core part is a rutile phase TiO_2 nanodendrite (ND) and the shell part is anatase or rutile phase TiO_2 nanoparticle deposited on the surface. The higher CB edge of the anatase phase in comparison to the rutile phase TiO_2 has an important part in the effective isolation of charges and suppresses charge recombination at the interfacial area. An optimum J_{sc} and utmost photoconversion efficiency of

$2.08\ mA/cm^2$ at $1.23V_{RHE}$ and 1.13% at $0.5V_{RHE}$ was obtained using this anatase/rutile 3D- branched TiO_2 photoanodes [237].

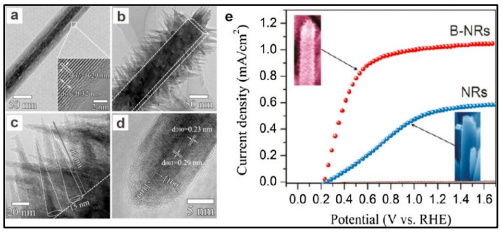

Figure 1.35: TEM image of (a) TiO_2 main trunk**,** (b, c) TiO_2 branches, (d) HRTEM image of a single branch, (e) LSV studies of unbranched and branched TiO_2 NRs photoelectrodes. [241]

Apart from branched TiO_2 nanostructure, some unique 3-D TiO_2 based photoelectrodes have also been reported in literature like nano-flowers, dandelion shaped, cross medal shaped, nanotress, and inverse opal nanostructure having outstanding PEC applications [214, 242-245]. Dong *et al.* synthesized Ti^{3+} self-doped flower-shaped partially reduced TiO_2 (R-TiO_2 NF_S) photoelectrode using a one-step hydrothermal approach followed by dipping in $NaBH_4$ (3M or 1M) aqueous solution. As compared with pristine TiO_2 nanoflowers (TiO_2 NF_S) the R-TiO_2 NF_S photoelectrode shows improved PEC activity, credited to the creation of Ti^{3+} and oxygen vacancy that extends the visible light response by squeezing the bandgap, ultimately increasing photoexcited carriers. The synthesized R-TiO_2 NF_S with dipping in 1M $NaBH_4$ shows an uppermost J_{sc} of $0.753\ mA/cm^2$ under AM 1.5 G irradiation and $0.183\ mA/cm^2$ at $0V_{SCE}$ beneath visible light irradiance that is 6 and 8 times higher than bare TiO_2 NF_S [246].

Cheng *et al.* synthesized a 3-D urchin-shaped hollow TiO_2/ZnO nanorod structure on FTO employing template assist technique, ALD, and hydrothermal method. The urchin-shaped TiO_2/ZnO photoelectrode was sensitized by CdS QDs for enhanced PEC

application. The as-synthesized CdS QDs sensitized urchin-shaped TiO_2/ZnO photoelectrode shows a maximum J_{sc} of $3.6\ mA/cm^2$ at $0V_{Ag/AgCl}$ due to enlarged surface area and better light scattering capability [247].

Zhu *et al.* synthesized 3-D lupines-like TiO_2/Sn_3O_4 nanosheets hierarchical heterojunction array (HHAs) using a two-step solvothermal growth process. The synthesized 3-D TiO_2/Sn_3O_4 HHAs photoanode shows an optimal J_{sc} of $1.05\ mA/cm^2$ at $0.79\ V_{RHE}$ is 3-fold higher than bare TiO_2 NRA photoanodes $(0.3\ mA/cm^2)$. Enhancement in PEC application is awarded to the increase in light-capturing capability, the maximum contact area with the electrolyte due to the high surface area, improved charge transport, and the synergetic effect amongst the band structure and the morphology [248].

Pathak *et al.* synthesized 3-D tree-shaped branched TiO_2 **(**bTiO_2) architecture through a hydrothermal approach. The synthesized bTiO_2 photoanodes were decorated with reduced graphene oxide (RGO) and CdS QDs **(**bTiO_2/RGO/CdS) and their PEC performance was investigated. The tree-shaped morphology of TiO_2 plays a prominent role in providing more surface area for the deposition of CdS and successful integration of RGO for efficient charge separation leading to an enhanced PEC performance. The synthesized bTiO_2/RGO/CdS photoanode shows an optimum J_{sc} of $3\ mA/cm^2$ [249].

Tian *et al.* successfully synthesized 3-D Cactaceae-shaped Anatase/Rutile (A/R) mixed-phase TiO_2 and employed it as a photoelectrode for PEC application. The mixed-phase A/R TiO_2 photoelectrode consists of ultra-thin (001) facet exposed anatase phase nanosheets grown on vertically aligned rutile phase TiO_2 NRA using a surfactant assistant approach **(Figure 1.36 a-d)**. Due to the synergetic effect of highly exposed (001) active facet and hierarchical heterojunctions, this peculiar morphology shows exceptional J_{sc} of $2.75\ mA/cm^2$ at $1.2\ V_{SCE}$ [250]**.**